The Journal of Chemical Physics

REVIEW ARTICLE | APRIL 12 2023

# Nucleation and growth of crystalline ices from amorphous ices

**Special Collection:** Nucleation: Current Understanding Approaching 150 Years After Gibbs

Christina M. Tonauer; Lilli-Ruth Fidler; Johannes Giebelmann; ... et. al



*J. Chem. Phys.* 158, 141001 (2023)
https://doi.org/10.1063/5.0143343

The Journal of Chemical Physics REVIEW scitation.org/journal/jcp

# Nucleation and growth of crystalline ices from amorphous ices

Cite as: J. Chem. Phys. 158, 141001 (2023); doi: 10.1063/5.0143343
Submitted: 22 January 2023 • Accepted: 15 March 2023 •
Published Online: 12 April 2023



Christina M. Tonauer, Lilli-Ruth Fidler, Johannes Giebelmann, Keishiro Yamashita, and Thomas Loerting[a)]

## AFFILIATIONS

Institute of Physical Chemistry, University of Innsbruck, 6020 Innsbruck, Austria

**Note:** This paper is part of the JCP Special Topic on Nucleation: Current Understanding Approaching 150 Years After Gibbs.
[a)]**Author to whom correspondence should be addressed:** thomas.loerting@uibk.ac.at

## ABSTRACT

We here review mostly experimental and some computational work devoted to nucleation in amorphous ices. In fact, there are only a handful of studies in which nucleation and growth in amorphous ices are investigated as two separate processes. In most studies, crystallization temperatures $T_x$ or crystallization rates $R_{IG}$ are accessed for the combined process. Our Review deals with different amorphous ices, namely, vapor-deposited amorphous solid water (ASW) encountered in many astrophysical environments; hyperquenched glassy water (HGW) produced from $\mu$m-droplets of liquid water; and low density amorphous (LDA), high density amorphous (HDA), and very high density amorphous (VHDA) ices produced via pressure-induced amorphization of ice I or from high-pressure polymorphs. We cover the pressure range of up to about 6 GPa and the temperature range of up to 270 K, where only the presence of salts allows for the observation of amorphous ices at such high temperatures. In the case of ASW, its microporosity and very high internal surface to volume ratio are the key factors determining its crystallization kinetics. For HGW, the role of interfaces between individual glassy droplets is crucial but mostly neglected in nucleation or crystallization studies. In the case of LDA, HDA, and VHDA, parallel crystallization kinetics to different ice phases is observed, where the fraction of crystallized ices is controlled by the heating rate. A key aspect here is that in different experiments, amorphous ices of different "purities" are obtained, where "purity" here means the "absence of crystalline nuclei." For this reason, "preseeded amorphous ice" and "nuclei-free amorphous ice" should be distinguished carefully, which has not been done properly in most studies. This makes a direct comparison of results obtained in different laboratories very hard, and even results obtained in the same laboratory are affected by very small changes in the preparation protocol. In terms of mechanism, the results are consistent with amorphous ices turning into an ultraviscous, deeply supercooled liquid prior to nucleation. However, especially in preseeded amorphous ices, crystallization from the preexisting nuclei takes place simultaneously. To separate the time scales of crystallization from the time scale of structure relaxation cleanly, the goal needs to be to produce amorphous ices free from crystalline ice nuclei. Such ices have only been produced in very few studies.



## I. INTRODUCTION

The great majority of $H_2O$ in our Milky Way is found as amorphous ice rather than as liquid water or crystalline ice (CI).[1,2] Amorphous ices may exist at temperatures below about 180 K and from ultrahigh vacuum conditions up to pressures of about 4 GPa.[3] In space, water condenses to amorphous ice from the gas phase or forms from mobile H, O, and OH moieties adsorbed on cold surfaces. Thus, amorphous ices cover interstellar dust grains,[4] comets,[5] or Saturn rings.[6] They play a pivotal role in protecting molecules from hard radiation in space by trapping them in its micropores.[7] Amorphous ices may even have carried the first amino acids to Earth in these trapping sites during the late heavy bombardment period about $4 \times 10^9$ years ago.[8,9] Closer to the Sun, in the zone above 150 K, amorphous ices may start to crystallize and release the trapped molecules. In the case of comets approaching the Sun, the crystallization of amorphous ice is directly connected with the outgassing of the trapped molecules, which contributes to both tails of a comet, the dust tail, and plasma tail. The rate of release of the trapped molecules is closely connected to the rate

of crystallization of amorphous ices. Yet, not very much is known about the rate of crystallization. It is clear, though, that the rate of crystallization differs very much depending on how the amorphous ices were formed and what their properties are. The porosities of amorphous ices may vary between 95% and 0%,[10] and specific surface areas of amorphous ices in the range of <0.1 and 280 $m^2\ g^{-1}$ have been reported.[11] A specific peculiarity of amorphous ices is their "polyamorphism," meaning that three different types of amorphous ices are known.[12–15] These amorphous ices are characterized in terms of different mass densities, which are 0.92, 1.15, and 1.25 g $cm^{-3}$ (all measured at 77 K and 1 bar) for the low density amorphous (LDA), high density amorphous (HDA), and very high density amorphous (VHDA) ice, respectively.[16] Other amorphous ices were claimed in the literature, such as intermediate-density amorphous (IDA) ice[17–19] and medium-density amorphous (MDA) ice,[20] but we do not consider them as polyamorphs. IDA cannot be equilibrated, which is a prerequisite for it being a polyamorph related to a liquid. Both IDA and MDA lack a glass transition in calorimetry scans, i.e., a transition to the deeply supercooled liquid is not observed. In the case of MDA, the procedure of milling crystalline ice is suggestive of MDA, in fact, being of nanocrystalline nature, where the nanosize leads to Scherrer-broadening of Bragg peaks in such a way that it cannot be distinguished from the halo of a truly glassy material. Nanocrystals are, therefore, x-ray amorphous, but there are no relation to glassy material and no nucleation and crystal growth in the glassy/deeply supercooled liquid going on that we discuss here in this Review. The three true polyamorphs LDA/HDA/VHDA differ by their distinct local binding motifs. Each water molecule in LDA is surrounded by four water molecules, forming a tetrahedral first hydration shell. LDA is also characterized by a well-defined second hydration shell that is clearly separated from the first shell. By contrast, for HDA and VHDA, the interstitial space between hydration shells is occupied by one and two water molecules, respectively. That is, the coordination number for LDA, HDA, and VHDA can be represented as 4+0, 4+1, and 4+2, respectively.[21] Interestingly, phase transitions between these three occur in a very narrow temperature-pressure interval and are characterized by sudden, step-like changes in properties such as density, coordination number, or isothermal compressibility.[15,22] Furthermore, the transitions can be reversed with hysteresis, a phenomenon typical for first-order transitions. Such phenomena occur despite amorphous ices being inherently non-equilibrium structures. In the temperature range of about 110–150 K, structural relaxation times of these non-equilibrium structures are on the second and sub-second time scale.[23] Using methods such as calorimetry,[24] volumetry,[25] or dielectric relaxation spectroscopy,[26] the glass transition temperatures $T_g$ have been reported as 116 K for HDA- and 136 K for LDA-type ices.[27] A key question that is still being discussed vividly and researched is whether or not HDA and LDA transform to deeply supercooled, ultraviscous liquids above these two distinct glass transition temperatures—which is the basis for two liquid theories of $H_2O$, aimed at explaining the anomalous nature of water in its supercooled state.[28–30] Upon heating beyond 150 K, it is still unclear whether or not amorphous ices crystallize from an amorphous solid or from a deeply supercooled liquid. In our previous work, we argue for the latter scenario,[31,32] where translational motions and diffusion are unlocked above the glass transition temperatures rather than merely local orientational motions.

In view of these open questions about the nature of amorphous ices near 150 K, it is surprising that there are only a handful of studies in which fundamental steps of crystallization are investigated directly, namely, nucleation and growth. Nonetheless, there are a significant number of studies in which crystallization of amorphous ices is tackled, where in most cases merely crystallization temperatures $T_x$ are reported. Going beyond that, there are a few studies in which crystallization kinetics are investigated.

In such studies, the kinetic model developed by Johnson, Mehl, Avrami, and Kolmogorov (JMAK) for isothermal phase transitions is usually applied.[33–38] It describes the crystallized fraction $f_{cryst}$ as a function of time $t$ at constant temperature as

$$f_{cryst}(t) = 1 - e^{-\frac{\pi}{3}\cdot J\cdot G^{n-1}\cdot t^n}, \tag{1}$$

where $J$ is the nucleation rate, $G$ is the growth rate and $n$ is the Avrami exponent with values between 1 and 4. In many cases, the value of $n$ allows for mechanistic interpretations of crystallization processes. Assuming that nucleation occurs in a one-dimensional manner, i.e., (idealized) "crystalline points" emerge within a matrix, the dimensionality of the crystal growth front is indicated by the value of $n - 1$. That is, a value of $n = 4$ represents the 3D-growth of (idealized) spherical crystalline grains, while $n = 3$ indicates the 2D-growth of plate-like grains. The fact that Eq. (1) contains three parameters ($J$, $G$, and $n$) means they are usually not obtained directly and unambiguously from fitting fraction $f_{cryst}$ as a function of $t$. Some authors combine nucleation rate $J$ and growth rate $G$ to a new parameter, i.e., the (combined) crystallization rate $R_{JG}$, simplifying Eq. (1) to

$$f_{cryst}(t) = 1 - e^{-R_{JG}\cdot t^n}. \tag{2}$$

Fitting measured $f_{cryst}(t)$ data with Eq. (2) and assuming a certain value for $n$ (e.g., $n = 4$ for nucleation and growth commencing within the bulk) yield values of crystallization rate $R_{JG}$ for a given temperature. Conversely, crystallization rates are accessible by measuring the reciprocal quantity, i.e., the (characteristic) crystallization time $\tau$. Including values for this parameter in Eq. (2) allows for the determination of the Avrami exponent $n$. The drawback of the simplification of Eq. (1) is the fact that the nucleation and growth kinetics cannot be separated. In this Review, we focus on experimental work, aimed at elucidating at least rates of crystallization. In some rare studies, experimentalists have attempted to separate the rate of crystallization into rates of nucleation, $J$, and rates of crystal growth, $G$.

This is a very difficult task, where the foremost challenge is the preparation of the amorphous ice itself. Depending on how the amorphous ice is made, it might contain a crystalline fraction to start with, nm-sized crystalline seeds, adsorbates or trapped impurities—all of which greatly affect $J$ and $G$. In addition, the microporosity and density of the amorphous ice vary very much with formation conditions. For this reason, we here attempt to group the results for the rates of crystallization in terms of the preparation path. Specifically, we distinguish between "amorphous solid water" (ASW) made by condensation of water vapor, "hyperquenched glassy water" (HGW) made by rapidly cooling $\mu$m-sized liquid droplets, and "low-density amorphous" (LDA) ice prepared from crystalline ice in a high-pressure setup, usually a piston-cylinder

setup or a diamond-anvil cell. These three amorphous ices all belong to the "LDA" and 4+0 coordination number category mentioned above. They differ in terms of morphology, where ASW contains micropores and HGW contains interfaces between individual droplets. LDA made in a piston-cylinder setup is considered as a fully compact sample, void of micropores, trapped molecules, or interfaces inside the sample. The only interface in LDA is its outer, geometric surface. Furthermore, we cover here the pressure range from the ultrahigh-vacuum to 6 GPa, where HDA and VHDA are the compact amorphous ices that are observed at high-pressure conditions. In this Review, the focus is fully on amorphous ices and the temperature range of up to 150 K (at ambient pressure) and of up to 190 K (near 2 GPa). We do not cover nucleation and growth in supercooled droplets in the temperature range between 273 and 200 K. Excellent reviews about nucleation and growth in such droplets are available in the literature,[39–42] in which the role of the internal Laplace pressure in nm- and $\mu$m-droplets is also discussed.

## II. NUCLEATION AND GROWTH IN VAPOR-DEPOSITED AMORPHOUS ICE (ASW)

Due to its non-equilibrium nature, vapor-deposited amorphous solid water (ASW) and its properties are highly dependent on the specific preparation path. Particularly in the last 25 years, experimentalists[10,43–64] have devoted much effort developing laboratory techniques targeting the open questions on crystallization and its key steps, i.e., nucleation and growth. ASW is usually deposited at UHV conditions ($<\sim10^{-8}$ mbar)[51,62,63] and analyzed *in situ* upon heating to temperatures above ~130 K. However, there are several experimental parameters that drastically influence the nature of ASW. The most important factors are schematically depicted in Fig. 1. Considering the deposition techniques, most literature studies either apply collimated molecular beam deposition at normal angle[51,62] or background deposition.[10,43,60] The former method yields dense, (mostly) non-porous films (Fig. 1, right). Background or backfill deposition describes deposition methods, where gaseous water molecules impact the support from all angles, resulting in microporous deposits with internal surface areas as high as 280 $m^2\ g^{-1}$[10,11,65] (Fig. 1, left). The influence of the deposition angle on porosity of the ASW film was meticulously studied in the past.[66–69]

In order to distinguish between (mostly) dense and microporous deposits, some authors refer to them as compact ASW (cASW) and porous ASW (pASW). The distinction between the two is, however, not straightforward. Upon heating, pASW experiences a collapse of its micropores, sometimes referred to as pASW to cASW transition. Yet, even cASW was shown to contain some pores with trapped molecules and a lamellar structure with some remaining pore volume between individual lamellae.[70] That is, one has to be careful about what the nomenclature "compact" or "non-porous" actually means. Quite often, also ASW samples described as such still contain a small number of remaining micropores or lamellar interfaces. It is also very hard to avoid impurities in ASW samples. They act like a cryo-pump and take up molecules from the background gas quite easily. Consequently, purities of ASW samples between different laboratories may be very different.[71]

Other factors for the preparation of ASW are the support itself, its material, and the temperature at deposition (Fig. 1, bottom). Furthermore, film thickness with its implication for crystallization kinetics is another hot topic.[44,50,54,63]

Figure 1 lists studies scrutinizing ASW films of different thicknesses from ~5 monolayers (MLs)[54,63] to 1050 bilayers (BLs)[50,51] (for more details, see Table I). Since there are differing statements on the conversion from ML or BL to nm (e.g., 1 ML ~ 0.3 nm[63] and 1 BL ~ 0.4 nm[50]), we refrain from converting the values in a uniform way, but rather cite them as they were reported in the literature.

Another factor that has to be considered upon the literature research on crystallization of ASW is the analytical method applied. Most authors use temperature-programmed desorption (TPD)[44,46,47,51,53,63] and/or reflectance/absorbance infrared spectroscopy (RAIRS).[10,54,57,60,62] Occasionally, other methods such as helium atom scattering (HAS)[53] and positronium annihilation spectroscopy (PAS)[56] have been applied. TPD utilizes the different sublimation tendencies of water molecules from amorphous and crystalline ice (CI), respectively. Ice I shows a lower sublimation rate due to its regular hydrogen bond network as opposed to ASW. Upon heating at a certain rate or keeping the film isothermally at certain temperatures (isothermal ITPD), crystallization changes the slopes in the respective desorption rate vs temperature[63] or vs time[44] diagrams. Crystallization of ASW also changes the desorption rate for other co-adsorbed molecules, e.g., $N_2$,[48] $CHF_2Cl$,[50] and $CHCl_3$,[52] which are therefore also applied for studying crystallization of ASW. The resulting "desorption spectra" are deconvoluted for their crystalline fraction at a certain temperature, which allows for an evaluation according to JMAK theory[33–38] [Eq. (1)]. One has to stress that this method is strictly surface sensitive. For probing the bulk, reflectance/absorbance infrared spectroscopy (RAIRS) is applied. The strong OH-stretching [or the decoupled OD] mode acts as a marker band to determine the crystalline fraction $f_{cryst}$ as a function of $t$ at certain temperatures, facilitating further analysis of the crystallization kinetics.

The plethora of parameters influencing the nature and properties of ASW (Fig. 1) makes the literature research on the nucleation of ASW tricky. As a result, there are several examples of seemingly contradictory results between different groups or even within the same group.[52,53,58,62,72] These cited studies, for example, treat the question whether ASW crystallization commences from the surface or within the bulk. On closer examination, differing results are not necessarily contradictory, but are a result of different initial samples (and/or conditions) and should therefore not be compared.

In Table I, the results of relevant studies conducted over the last 25 years on crystallization of ASW are summarized.

These studies cover the temperature range 126–235 K and show activation energies for the combined nucleation and growth process $E_{JG}$ range between 43 and 92 kJ $mol^{-1}$. Crystallization was studied from the nanosecond-timescale at the high-temperature end to the hours-timescale at the low-temperature end. The most important topics, such as the kinetics of crystallization as a function of film thickness, the question whether nucleation starts at the surface or the bulk, the influence of morphology, and finally the disentanglement of nucleation and growth as separate processes over the course of crystallization, shall be discussed in the following.

**TABLE I.** Comparison of experimental parameters and results from different authors studying crystallization of ASW. Superscript * denotes apparent growth/nucleation rates which where not obtained in independent experiments and therefore may be intertwined.

| Authors | Deposition method | Thickness | Analysis methods | Crystallization time $\tau$ (s) | Nucleation rate $J$ ($m^{-3}$ $s^{-1}$), Growth rate $G$ (Å $s^{-1}$) or Crystallization rate $R_{JG}$ | Crystallization temperature $T_x$ (K) | Activation energy (kJ $mol^{-1}$) | Avrami exponent n |
|---|---|---|---|---|---|---|---|---|
| Smith *et al.*[44] | Molecular beam, Ru(001), Au(111), 85 K | 5–80 ML | TPD (QMS) | 48 (160 K) | N/A | 156-166 | $E_{JG}$ = 84 | 4 |
| Dohnálek *et al.*[48] | Molecular beam Pt(111), 22 K | 10–45 BL, 150 BL | TPD of $N_2$, $H_2O$ | $\tau_{1/2}$ (135 K): $2 \cdot 10^3$ s (22 BL), $9 \cdot 10^3$ s (34 BL) | N/A | 129–135 (15 BL), 140–146 (150 BL) | $E_{JG}$ = 77 ± 1<br>$E_G$ = 56 ± 2<br>$E_J$ = 140 ± 10 | 4.2 ± 0.4 |
| Safarik *et al.*[50] | Molecular beam, Ir(111), 77 K | 150–1050 (~55–385 nm) | TPD of $CHF_2Cl$ | N/A | 136 K: $J^*$=5.5 · $10^{15}$/$G^*$=0.30<br>140 K: $J^*$=6.5 · $10^{16}$/$G$=1.5 | 136–140 | $E_G^*$ = 68 ± 6<br>$E_J^*$ = 100 ± 20 | 3–4 |
| Safarik and Mullins[51] | Molecular beam, Ir(111), 77 K, seeding at 142 K | 150–1050 BL (~55–385 nm) | TPD of $CHF_2Cl$ | N/A | 134 K: $J$ = 3.$10^{13}$/$G$ = 0.4<br>142 K; $J$ = 2.$10^{17}$/$G$ = 4 | 134–142 | $E_G$ = 47 ± 2<br>$E_J$ = 168 ± 13 | 4 |
| Backus *et al.*[52] | Molecular beam, Pt(533), 100 K | 45 ML | RAIRS, TPD of $CHCl_3$ | 500 (139 K) | $J_{surf}^*$ = 5.5 · $10^{-7}$ $ML^{-2}$ $s^{-1}$/$G^*$ = 0.31 | 139 K | N/A | N/A |
| Kondo *et al.*[53] | Backfill vapor deposition, Ru(001), 90 K | 50 ML | HAS, RAIRS, TPD | N/A | $J^*$ = 7.2 · $10^{-9}$–4 · $10^{-6}$ $ML^3$ $s^{-1}$<br>$G^*$ = 4.3 · $10^{-2}$–0.25 ML $s^{-1}$ | 152–160.6 | $E_{JG}$ = 63 ± 2<br>$E_G^*$ = 42, $E_J^*$ = 151 | 3.5 |
| Yamauchi *et al.*[54] | Vapor deposition via 1 mm capillary, Ru(001), 84 K | 8, 11, 25 ML | RAIRS, ITPD | 840 (147 K, 11 ML), 180 (150 K, 8 ML) | $k_{JG}$: 147 K: 2.1 ± 0.8 · $10^{-3}$ $s^{-1}$<br>150 K: 10.5 ± 3.3 · $10^{-3}$ $s^{-1}$ | 147–150 | $E_{JG}$ = 92 ± 3 | 1.88 ± 0.10 (147 K, 11 ML) |
| Maté *et al.*[10] | Background deposition, Si, 14/40/90 K, porous (280 $m^2$ $g^{-1}$) | ~100 nm | FTIR | N/A | $k_{JG}$: 14 K-deposit: 8.8 + 1.0 · $10^{-4}$ $s^{-1}$<br>40 K-deposit: 6.6 + 2.5 · $10^{-4}$ $s^{-1}$<br>90 K-deposit: 6.3 + 0.4 · $10^{-4}$ $s^{-1}$ | 150 | N/A | 1.00/2.04/2.17 for 14/40/90 K-deposit |
| Mitchell *et al.*[60] | Background and angle-dependent 0°–70° deposition, CsI, 10 K | ~1000 ML | FTIR | 136 K: 5 · $10^3$ (9% porosity), 3 · $10^2$ (43% porosity) | $k_{JG}$: external surf.: 0.5–100 · $10^{-6}$ $s^{-1}$<br>internal surf.: 2–30 · $10^{-4}$ $s^{-1}$ | 130–141 | internal surf.: 64 ± 3/60 ± 3 (9%/43% porosity) | external surf.: 0.4–0.7; internal surf.: 4–1.5 |
| Xu *et al.*[59] | Molecular beam on Pt(111), 90 K, 10 ns-pulse heating | 240 nm | RAIRS | N/A | $J$ = $10^{26}$–$10^{29}$/$G$ from Ref. 57 | 210–225 | N/A | 4 |
| Kimmel *et al.*[62] | Molecular beam, Pt(111), 90 K, 10 ns-pulse heating | 50–100 ML (15–30 nm) | RAIRS | N/A | $J$ (216 ± 4 K) = $10^{29}$ $G(T_{pulse}$ = 244 K) ~ 4 Å/pulse | 185–235 | N/A | 4 |
| Harada *et al.*[63] | Backfill vapor deposition, Pt(111), 110/135 K, non-porous | 9, 18, 27, 45 ML (1 ML = 0.3 nm) | RAIRS, TPD | N/A | $k_{JG}$ (145 K): 9 ML: ~0.01 $s^{-1}$ 18 ML: ~0.003 $s^{-1}$ | 145 K | $E_{JG}$ (5 ML, where $n$ = 1): $E_{JG}$ = $E_N$ = 43 ± 3 | from 1 to 4<br><20 ML: 1-4,<br>>20 ML: 4 |

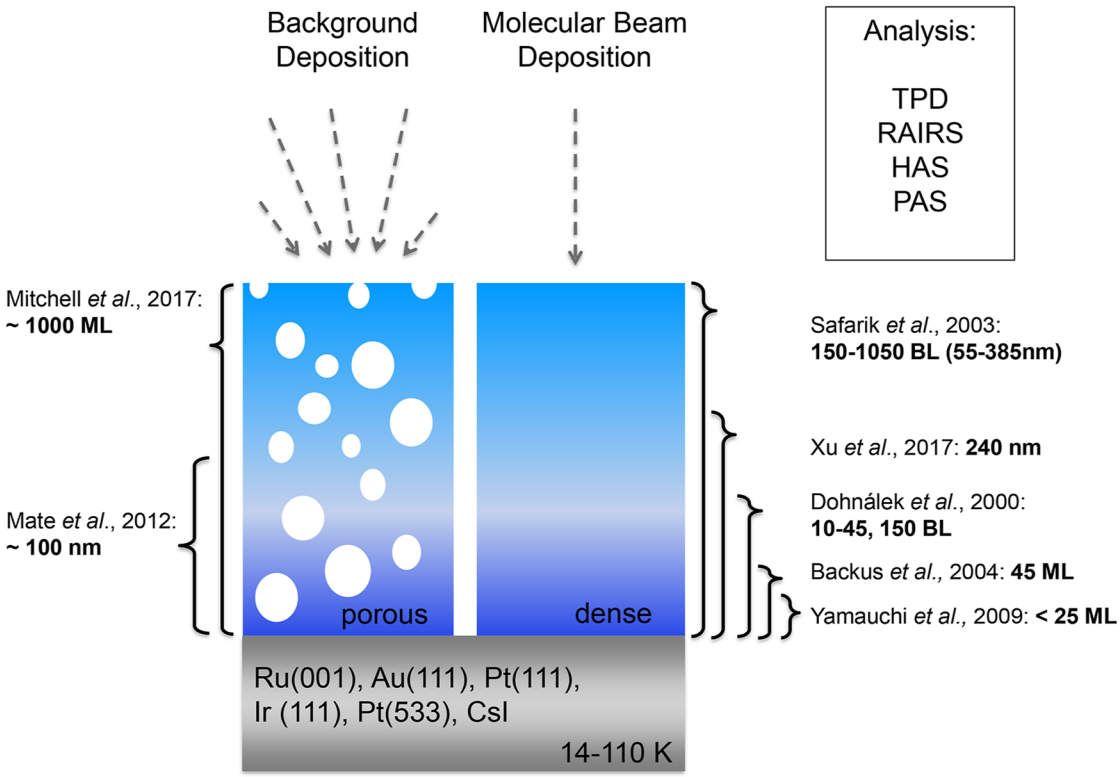


**FIG. 1.** Schematic depiction of two types of ASW films deposited on a substrate with experimental parameters indicated.

### A. Influence of film thickness and substrate

In their study on desorption and crystallization in nanofilms of ASW at 156–166 K, Smith *et al.* applied ITPD.[44,46] They scrutinized the influence of different single crystal substrates [Ru(001) and Au(111)], the thickness of the deposited ASW film (5–80 ML), and temperature on the (surface) crystallization time $\tau$. Independent of the substrate, $\tau$ increases with the thickness of the film until it reaches a saturation value. They described the film thickness dependence of $\tau$ as follows:

$$\tau = \tau_\infty \left(1 - e^{-\frac{L}{L^*}}\right), \tag{3}$$

where $\tau_\infty$ and $L^*$ are fit parameters. They reported a value of $L^*$ = 15 molecular layers (~5 nm). They interpreted $L^*$ as the average distance between nucleation embryos in the amorphous material. According to their interpretation, in films thinner than $L^*$, the probability of (bulk) nucleation and the resulting number of nucleation embryos are low and rather constant upon increasing the film thickness up to $L^*$. Thus, below $L^*$, (surface) crystallization is limited by the number of nuclei present in a thin film. As a result, (surface) crystallization slows down linearly with the increasing thickness. Above $L^*$, nucleation is no limiting factor for crystallization, resulting in a plateau of crystallization time $\tau$. However, one must consider that the authors applied the surface-sensitive method of ITPD. Therefore, their observation does not necessarily apply to the bulk. Dohnálek *et al.*[47,48] reinterpret the slowing down of crystallization with the increasing film thickness to be a result of crystallization-induced cracking of the ASW films. They stated that, because of the cracks, there is less contact between grains and the surrounding amorphous phase, slowing down crystallization.

In the study of Smith *et al.*,[44,46] crystallization time $\tau$ shows Arrhenius-like behavior with the temperature of the substrate, resulting in a substrate-independent activation energy of 84 kJ mol$^{-1}$. By modeling the fraction of amorphous and crystalline ice in their isothermal desorption spectra (desorption rate vs time), they found the best curve fit when including an Avrami exponent $n$ = 4. This implies a constant nucleation rate everywhere in the sample and isotropic 3D growth of the nuclei in nanofilms of ASW. To sum up, they found that the crystallization kinetics of ASW are strongly dependent on both temperature and film thickness and are consistent with a spatially random nucleation and isotropic growth model, but independent of the metal support.

However, crystalline ice as a substrate acts as a 2D nucleus for crystal growth, even at temperatures below 110 K.[47,48] In their subsequent studies, Dohnálek *et al.*[47,48] studied crystallization of ASW with and without crystalline ice as a growth nucleus. They compared crystallization of pure ASW films (involving both nucleation and growth) and crystallization of ASW on top of a crystalline ice template (governed by growth). This comparison allows

for the determination of activation energies for ice nucleation $E_J$ (140 kJ mol$^{-1}$) and growth $E_G$ (56 kJ mol$^{-1}$). These experiments are the foundation for the subsequent "intentional seeding" experiments, aimed at separating nucleation and growth, discussed below.[51,59,62]

Safarik *et al.*[50] studied (surface) crystallization in thicker films than the ones prepared by Smith *et al.*,[44,46] Löfgren *et al.*,[49] and Dohnálek *et al.*[47,48] (<150 BL, 55 nm). They applied 150–1050 BL (55–385 nm) thick ASW films using the surface-sensitive method of TPD of $CHF_2Cl$. They fitted their isothermal crystallization data at $T$ = 136–140 K with an Avrami-like model they had developed for surface transitions.[73] When comparing 150, 300, and 1050 BL (55, 110, and 385 nm) films, they reported that surface crystallization, in fact, accelerates with thickness in this particular range. Considering the earlier results from the work of Smith *et al.*[44] and Löfgren *et al.*,[49] Safarik *et al.*[50] suggested a broad maximum of crystallization time between 70 and 150 BL thick films. They rationalized the finding with the idea that in this range 3D-growth of (idealized) spherical crystallites is geometrically limited in the direction perpendicular to the support. For thicker films (>150 BL), grains of larger radius and grains nucleated further away from the surface (at higher "nucleation depth") can grow and impinge on the surface, contributing to accelerated surface crystallization.

Combining the earlier observations on thinner films[44,46,49] [slowing down of (surface) crystallization with the increasing film thickness and reaching a plateau of $\tau$ below 55 nm] with the ones of Safarik *et al.*[50] [acceleration of (surface) crystallization above 55 nm] and given that the samples are void of any inhomogeneities leads to the tentative assumption that there might be three regimes of film thicknesses: (1) the "thin film regime" where crystallization is limited by nucleation, (2) the "intermediate film regime" where crystallization times show a plateau (or broad maximum) due to the geometrical limitation of grain growth, and (3) the thick film regime with again accelerated crystallization where grain growth is merely limited by collisions with other grains.

Yamauchi *et al.*[54] studied the very thin film regime of ~10 ML of ASW on Ru(001) using both isothermal TPD and RAIRS. Their JMAK evaluation exhibits exponents of $n \sim 2$. This suggests that ASW crystallization for very thin films, in fact, proceeds through 1D random nucleation and growth. This finding is confirmed in the recent work of Harada *et al.*,[63] Fig. 2. They scrutinized the film-size dependent crystallization of 9–45 ML ASW on Pt(111) (the same range as in Refs. 44, 48, and 54), but used TPD (surface) and RAIRS (bulk) simultaneously. They also found a decrease in the crystallization rate with the film thickness in the range below 45 ML. Furthermore, they identified an increase of crystallization temperature with the thickness below 20 ML for both $H_2O$ and $D_2O$ deposits. The Avrami exponent $n$ increases from ~1 (at ~5 ML) to 4 (at ~20 ML). In other words, at only 5 ML, growth is 0-dimensional, and crystallization is governed by nucleation only. They approximated a value for the nucleation activation energy $E_J$ at 5 ML since the (combined) crystallization activation energy $E_{JG} = E_J$ if $n = 1$.[63] However, their value of 43 kJ mol$^{-1}$ (Table I) seems low compared to 140 kJ mol$^{-1}$ deduced by Dohnálek *et al.* and others[48,51,53] (Table I). Harada *et al.* estimated the critical nucleus size (diameter) to be only ~5 molecules (1.5 nm) at ~130 to 150 K.[63] For comparison, Lupi *et al.* reported in their theoretical study on nucleation of mW water a critical ice nucleus size of ~450 molecules at the homogeneous nucleation temperature of 230 K.[74] On the other hand, the study of Harada *et al.* shows that a thickness of 20 ML marks the onset of a bulk regime where ASW crystallizes homogeneously and features random nucleation and 3D growth.

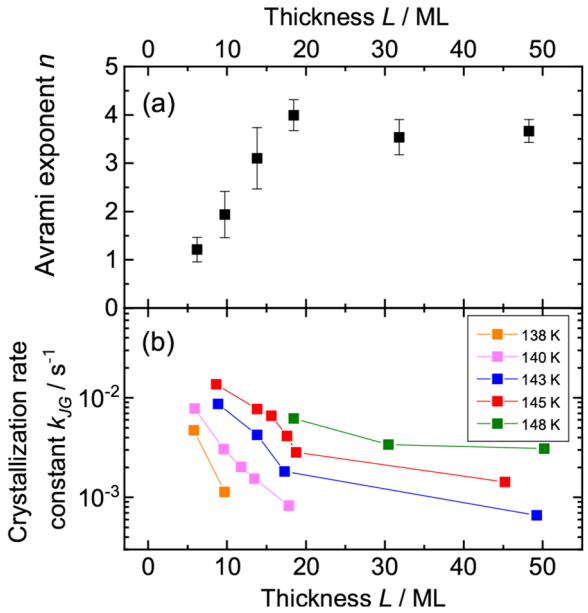


**FIG. 2.** (a) Avrami exponent $n$ and (b) crystallization rate constant $k_{JG}$ as a function of ASW film thickness $L$ (1 ML ~ 0.3 nm), data extracted from the work of Harada *et al.*[63]

In order to explain the thickness-dependence of crystallization (<20 ML), Harada *et al.* compared the width of the decoupled HDO stretching mode. They derived a distribution of intermolecular H-bond lengths with film thickness. According to that analysis, thinner films contain a larger fraction of both short and long hydrogen bonds than thicker films (>20 ML). That is, the thinner film shows a larger variation of H-bond lengths and a higher degree of disorder.

## B. Surface vs bulk nucleation and crystallization

While most authors reported crystallization emerging from the bulk,[44,45,48,51,53,62–64,75] there are a few reports of surface-initiated crystallization.[52,58,72] Backus *et al.*[52] investigated 45 ML ASW films using RAIRS and TPD of $CHCl_3$. Upon comparing the crystallized fraction at the surface (TPD) and bulk (RAIRS) at 139 K, they found that 73% of the surface but only 63% of the bulk had converted. They rationalized the finding with surface-induced crystallization. In contrast, Harada *et al.*,[63] applying TPD (without probe molecule) and IR spectroscopy, found that crystallization in the bulk and at the surface occurs simultaneously on the experimental timescale of 40 s. They also put forward the fact that $CHCl_3$, used by Backus *et al.*,[52] has a much higher desorption temperature (130–145 K) than the gases typically used for TPD[63] [$N_2$ (25–45 K) in the Kay/Kimmel group[47,48] and $CHF_2Cl$ (85–105 K) in the Mullins group]. Due to the stronger interaction between $CHCl_3$ and ASW and based on literature studies about $CHCl_3$[76] and HCl[77] on ASW,

Harada *et al.* suggested that surface crystallization in the study of Backus *et al.*[52] was stimulated by the probe molecule $CHCl_3$ itself and is not a result of preferential formation of crystalline nuclei at the surface.[63]

Yuan *et al.* also have targeted the question whether crystallization propagates top-down from the surface to the bulk or vice versa.[58] According to this study, the surface crystallization time is independent of film thickness at least in the range of 100–1000 ML, while the crystallization time in the bulk increases linearly with film thickness. By preparing selectively H/D exchanged ASW layers, they showed nucleation and crystallization of ASW to start at the solid/vacuum interface. They rationalized this with an increased mobility at the surface. In a follow-up study, they compared crystallization kinetics of nanoscale films of ASW either on top of a decane layer or sandwiched between two layers without an ASW/vacuum interface.[72] Adding a layer of decane on top of ASW suppresses surface nucleation and crystallization, resulting in approximately eight times slower crystallization times. Harada *et al.*,[63] however, argued that a thick decane substrate might lead to significant heat accumulation during deposition. Less efficient dissipation of heat could possibly lead to some local heating at the ASW/vacuum interface and, therefore, be responsible for the observed top-down crystallization.

### C. Morphology—Porous vs compact ASW

The question about the influence of morphology on the crystallization of ASW is often raised in the context of astrophysical implications of ASW.[10,43,60] Maté *et al.*[10] scrutinized isothermal crystallization of ASW at 150 K, prepared via background deposition at 14, 40, and 90 K, respectively. Lower deposition temperature results in higher porosity.[78] Their Avrami evaluation of the evolution of the HDO band upon crystallization shows an Avrami exponent of ~1 for samples deposited at 14 K and ~2 for the samples deposited at 40 and 90 K. The difference between these values and the ones observed for dense ASW samples (~4; see Table I) hints at the idea that different nucleation/growth processes are involved in porous ASW (pASW) as opposed to dense/compact ASW (cASW). Safarik and Mullins[51] suggested that sublimation and recondensation of water molecules in the micropores might be the fundamental process in porous ASW that leads to crystalline ice. In dense ASW, this mechanism can no longer take place so that in cASW, the crystallization takes place in the solid state itself rather than via the vapor phase. However, Harada *et al.*[63] reported no difference between the crystallization kinetics of porous and non-porous ASW samples [distinguished by different (background) deposition rates in their study[63]], referencing the work of Smith *et al.*[79] However, even the so-called "non-porous" ASW [prepared by directed deposition at a deposition angle of 0° (Fig. 1, right)] still contains pores, as shown by Mitchell *et al.*[60] Therefore, the observation of Harada *et al.*[63] likely emanates from the fact that they compared samples of possibly similar porosity rather than comparing porous with "non-porous" ASW.

In their crystallization study on porous ASW, Mitchell *et al.*[60] reported two distinct stages of crystallization. The first stage (responsible for ~10% of the transformation) involves nucleation at the external surface, while the second, faster stage commences from the internal pore surface. They also showed that fivefold porosity results in ~15 times faster crystallization kinetics. Their separate analysis of

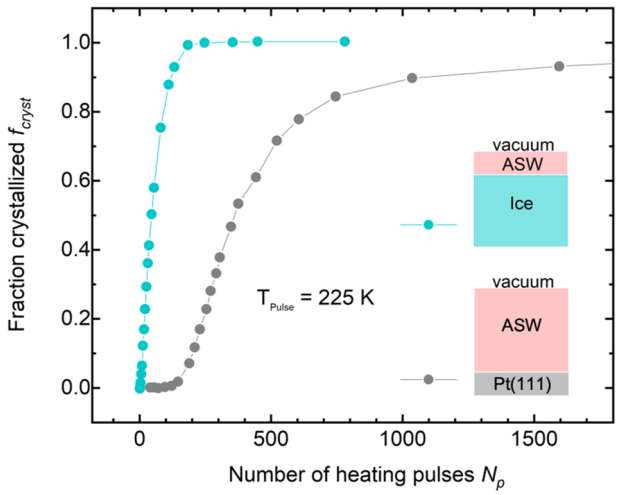


**FIG. 3.** Fraction of crystallized ice $f_{cryst}$ vs number of ns-pulses $N_p$ upon transiently heating ASW films to 225 K (equivalent to the time axis in a typical Avrami plot). The gray dataset represents a sigmoidal curve governed by both nucleation and growth, typical for crystallization of ASW (100 ML) deposited onto a metal support [Pt(111)]. Note the flat induction period representing nucleation ($<N_p$ = 200), the steep increase representing the growth of nuclei, and the plateau at the end, indicating completeness of crystallization. The turquoise dataset shows a curve typical for ASW crystallization catalyzed by a crystalline ice template underneath the ASW film (25 ML ASW on top of 75 ML crystalline ice). In this case, crystallization is governed by the growth process right from the beginning, whereas the flat induction period is missing. Data extracted from supporting information, Fig. S5 of Ref. 57.

the different crystallization modes results in Avrami exponents of $n_1$ ~ 0.4–0.7 (first stage) and $n_2$ ~ 4–1.5 (second stage), decreasing with the increasing porosity. Similar to the interpretation of Safarik and Mullins,[51] Mitchell *et al.*[60] suggested that the second crystallization stage is due to the nucleation in the interior of the ice at the surface of pores.

### D. Disentangling nucleation and growth

Based on the fact that nucleation is inherently hard to access, measurements of absolute values for nucleation rates of ASW are scarce. Conducting isothermal crystallization experiments and plotting the converted fraction vs time (similar to Fig. 3) make a fit with the JMAK-model possible.[33–38] However, usually, the combined nucleation and growth rate is obtained as a fit parameter, not allowing for an unambiguous determination of both of them independently.

In order to separate nucleation from growth, researchers have come up with a sophisticated strategy:[48,51,57,59,62] they have intentionally "seeded" their ASW films with crystalline ice. As a result of "prenucleation,"[51] the crystallization process is governed by crystal growth only, allowing for a direct measurement of growth rates. Furthermore, these values are used as non-adjustable parameters in the JMAK model [Eq. (1)], allowing for a separate determination of nucleation rates.

In a first set of experiments, Safarik and Mullins[51] intentionally "seeded" ASW films with crystalline nuclei by annealing samples for 450 s at 142 K, prior to isothermal crystallization experiments

at $T$ = 134–138 K. The second set of experiments is conducted with pure, seed-free samples, much like in Ref. 50. The comparison of the resulting Avrami plots exhibits an immediate steep linear increase for prenucleated datasets, while the pure samples show typical sigmoidal curves with an initial induction time (time lag), where crystallization kinetics are governed by an interplay of nucleation and growth (see Fig. 3). The combination of these two model fits of the two distinct sets of experiments allows for the determination of nucleation rates between 134 and 142 K and nucleation activation energy $E_J$ (Table I). They pointed out good agreement between their results and the ones of Dohnálek *et al.*[47,48] However, there is a discrepancy with the results of Jenniskens and Blake,[43] showing a much smaller activation barrier for nucleation (41 kJ mol$^{-1}$) compared to their value of 168 kJ mol$^{-1}$. They rationalized this difference by the different ASW morphology, where compact films are produced by Safarik and Mullins[51] and Dohnálek *et al.*,[47,48] but porous films are produced by Jenniskens and Blake.[43]

In 2019, the Kay/Kimmel group published two studies targeted at the disentanglement of nucleation and growth in the crystallization process of thin ASW films,[61,62] similar to their earlier studies.[57,59] Their approach was to "use a 2D nucleus as a seed for crystal growth,"[47,48] i.e., a crystalline ice substrate underneath ASW. Furthermore, they employed a 1000 ML ASW film, containing layers of isotope-exchanged ASW (5% $D_2O$ in $H_2O$) at different positions within the film. These isotopically substituted layers enabled them to locate the propagating crystalline front by using RAIRS. The films either had a "free" interface with the vacuum or were capped with an organic layer.[72] In isothermal experiments at temperatures between 140 and 150 K using RAIRS, they expectedly observed a steep rise in the Avrami plots [$f_{cryst}(t)$, comparable with Fig. 3] with no initial induction time. From this slope (after converting the crystalline fraction axis to "crystallized monolayers," Fig. 4), they were able to extract temperature-dependent growth rates, e.g., 2.7 ML/s at 150 K. In addition, they reported an activation energy for growth $E_G$ of 40 ± 3 kJ mol$^{-1}$.[61] In order to probe $J$, they applied ~10 ns laser pulses to transiently heat 15–30 nm films of ASW to 188–230 K at ~$10^9$ to $10^{10}$ K s$^{-1}$.[62] Kimmel *et al.* proposed that transiently heating thin ASW films allows for exploring bulk (homogeneous) nucleation in deeply supercooled liquid water. This is because their experiments showed no significant difference between crystallization of "free" and "capped" water films. Accordingly, surface nucleation and crystallization play a minor role of in this setup. Since they were able to obtain growth rates as a function of temperature in independent measurements, they were able to determine nucleation rates by modeling their observed crystallization kinetics using JMAK theory. Their experiment suggests a maximum of $J$ at ~216 K at $10^{29\pm1}$ m$^{-3}$ s$^{-1}$ and a rapid drop by 4–5 orders of magnitude at 189 K (Fig. 5). However, quite recently, de Almeida Ribeiro *et al.* proposed that transient heating experiments using ns-pulses suffer from unclear temperatures.[80] Based on their molecular simulations, they questioned whether the structure probed after the ns-pulse is, in fact, representative of the structure at $T_{pulse}$. This might imply some degree of uncertainty along the $T$-axis in Fig. 5.

Figure 5 summarizes nucleation rates as a function of temperature from different studies.[62] The work of Xu *et al.*[59] on thicker films (240 nm) shows a decrease of $J$ with the increasing temperature, in accordance with a maximum between 210 and 220 K. Between 230 and 240 K, data on ice nucleation from $\mu$m-sized droplets are

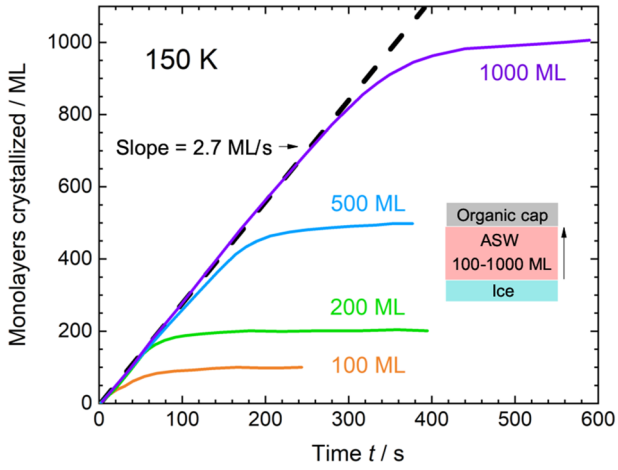


**FIG. 4.** Time dependence of crystallization for four different ASW films (between 100 and 1000 ML thickness) sandwiched between a crystalline ice template (bottom) and an organic cap (top). This sandwich structure allows for selective bottom-up crystallization (as indicated by the arrow) and growth rate determination, monitored by isothermal RAIRS measurements. Data taken from Ref. 61.

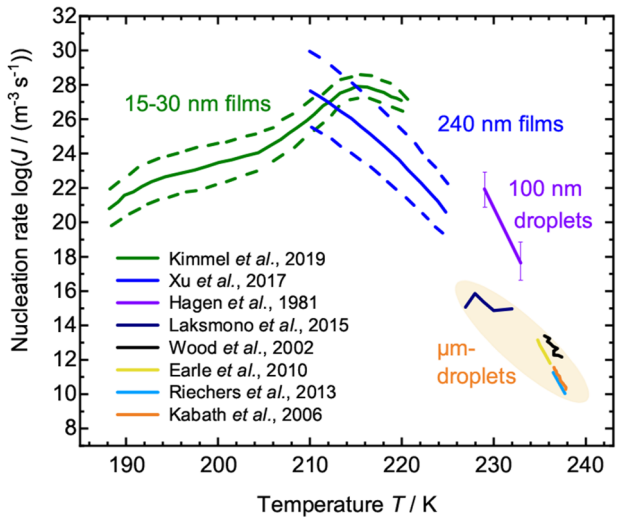


**FIG. 5.** Summary of nucleation rate data in thin ASW films in the range 188–224 K and in nm- and $\mu$m-sized liquid droplets in the range 227–238 K, adapted from Ref. 62.

presented (Hagen *et al.*: 0.1 $\mu$m,[81] Laksmono *et al.*: 9–12 $\mu$m,[40] Wood *et al.*: 35 $\mu$m,[82] Earle *et al.*: 1–2.9 $\mu$m,[83] Riechers *et al.*: 53–96 $\mu$m,[84] and Kabath *et al.*: 30–100 $\mu$m[85]). The different studies carried out above 235 K show a remarkably similar trend and seem like an extrapolation of the data from the work of Xu *et al.*[59] However, the experiments of Hagen *et al.*[81] at 225–235 K differ significantly from the ones of Laksmono *et al.*[40] (Fig. 5). A plausible explanation for the difference is the much smaller droplet dimension in the experiments of Hagen *et al.*[81] compared to Laksmono *et al.*[40] The resulting increase of Laplace pressure for the smaller droplets

of 100 nm may shift the nucleation rates to higher values compared to the ones obtained by Laksmono *et al.*[40] Laplace pressures are on the order of 100 MPa in the interior of droplets of 2 nm, but rather small for 100 nm droplets.[86] Such high pressures lower the degree of supercooling and, hence, suppress nucleation.[87] This is confirmed in the mW model.[88,89] At the surface of nanodroplets, pressures are on the other hand negative, thereby enhancing nucleation.[90] That is, surface nucleation is preferred in nanodroplets, whereas in thin films, bulk nucleation is preferred. Yet, the complicated nature of nucleation in nanodroplets is not clear and needs further investigation.[90] The difference between the experiments of Hagen *et al.*[81] and Laksmono *et al.*[40] might, therefore, also be caused by other effects, especially preseeding that is only of relevance in the amorphous films, but not in nanodroplets.[40,89]

## III. NUCLEATION AND GROWTH IN HYPERQUENCHED GLASSY WATER (HGW)

The straightforward way to form a glass is to cool the melt rapidly to avoid crystallization.[91] In the case of water, this has proven to be rather difficult. Even high cooling rates, often realized by directly plunging samples into liquid nitrogen, do not suffice by far to vitrify pure water.[92,93] Instead, crystallization intervenes, and the glassy state is not reached. Due to this circumstance, aqueous solutions are often used instead. They vitrify more easily since the addition of substantial amounts of solutes increases the configurational entropy and greatly reduces rates of crystallization.[92,94] In more dilute aqueous solutions, the rates of crystallization are still too high so that plunging into liquid nitrogen still results in crystallization rather than vitrification.

Brüggeller and Mayer were the first ones to actually reach the cooling rates necessary to vitrify pure liquid water.[13] In their first successful attempts, they used a jet of micrometer-sized liquid water droplets and *n*-heptane as a cryomedium. By contrast to liquid nitrogen, *n*-heptane is a non-boiling cryomedium, where evaporation does not avoid the direct contact of water droplets with the cryomedium. That is, the "Leidenfrost effect" is an issue for liquid nitrogen, but not for liquid *n*-heptane. However, the major disadvantage of the latter cryomedium is the difficulty to separate the vitrified water from *n*-heptane without contamination. Facing this issue, Mayer discovered another way to vitrify liquid water, which is referred to as hyperquenching.[95] Here, micrometer-sized liquid water droplets are injected into a high-vacuum chamber, develop ultrasonic speed, and hit on a cooled copper substrate, on which every single droplet immediately turns into a glassy droplet. The glassy deposit is called hyperquenched glassy water (HGW). HGW usually contains less than 5% crystalline material[96,97] and consists of 3 $\mu$m-sized glassy droplets stacked upon each other to form a ~1 mm thick volcano-shaped deposit.[97] The droplets are cooled from 300 to 77 K in ~20 $\mu$s, which beats the timescale of crystallization. Yet, the density of the droplets decreases from 1.00 g cm$^{-3}$ at 300 K to 0.92 g cm$^{-3}$ at 77 K. That is, even on this timescale, there are significant fluctuations of density upon cooling. It seems plausible that this is due to the crossing of the Widom line[98] (near 220 K at vacuum conditions), below which the low-density liquid (LDL) is more stable than the high-density liquid (HDL). That is, density fluctuations drive the liquid into a state that is 9% less dense than liquid water at ambient temperature. To suppress such fluctuations, even faster cooling than currently achieved in the hyperquenching experiments of ~$10^7$ K s$^{-1}$ is required. In these 20 $\mu$s cooling time, also the glass transition temperature of 136 K[99] is crossed so that the glassy deposit called HGW according to its preparation route belongs to the category of low-density amorphous (LDA) ice.

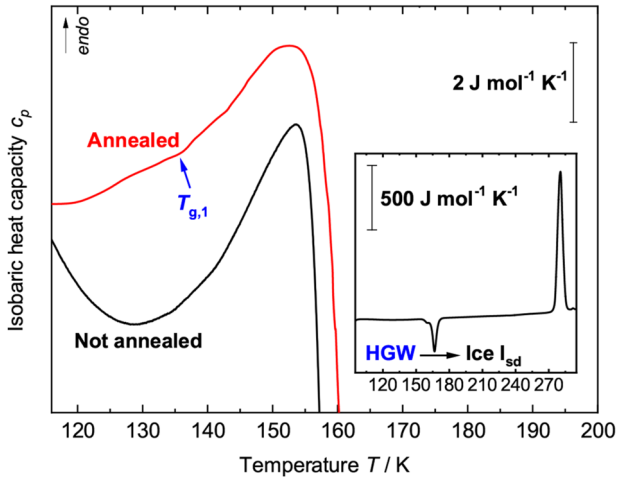


**FIG. 6.** Heating traces of HGW at ambient pressure employing a heating rate of 30 K min$^{-1}$. Traces for annealed (red curve, extracted from Ref. 100) and unannealed HGW (black curve, measured by us) are shown. $T_{g,1}$ marks the glass transition temperature of annealed HGW. In the case of unannealed HGW, $T_{g,1}$ is masked by a broad exotherm that signifies enthalpy relaxation.[100] The inset shows a zoom-out (note the scale bars) of the black curve showing the crystallization exotherm (onset temperature ~152 K) and the melting endotherm (onset temperature 273 K).

Without the cryomedium, calorimetric *ex situ* heating experiments were finally possible, which revealed the thermal behavior of HGW. Figure 6 shows an example of the observed behavior of HGW upon heating using differential scanning calorimetry (DSC). Without annealing (black trace in Fig. 6), HGW experiences first a continuous enthalpy relaxation between 100 and 140 K, which is followed by a sharp exotherm between 160 and 170 K (inset of Fig. 6).[101] This indicates crystallization to ice I, more specifically to stacking disordered ice I ($I_{sd}$) that contains both cubic and hexagonal stacking sequences. Annealing the sample, for instance, for 90 min at 129 K, allows the sample to slowly release enthalpy and to reach the metastable equilibrium state before the actual DSC scan is carried out. The red trace in Fig. 6 represents the DSC scan after the annealing step. The glass transition is observed right before the onset of the crystallization. The widely accepted literature value of $T_{g,1}$ (the glass transition temperature at the LDA/LDL transition) at 30 K min$^{-1}$[101] is 136 K. The crystallization temperature $T_x$ also depends on the heating rate and was found at 158.5 K for 10 K min$^{-1}$[99] and 150 K for 30 K min$^{-1}$.[101] In addition, the $D_2O$ isotope effect of has been investigated, where deuterated samples show slower kinetics and higher crystallization temperature, namely, 156 K when heating with 30 K min$^{-1}$.[102]

### A. Crystallization kinetics of vitrified droplets (HGW)

Detailed studies on the crystallization kinetics of HGW are scarce probably because very specialized experimental equipment is

needed to recover the glassy deposit and to do subsequent *ex situ* experiments. In addition, computational studies on that topic are quite demanding because of low temperatures and long time scales involved.[89,103,104] In any case, quantifying the kinetics of crystallization usually involves isothermal crystallization experiments (or simulations).[10,89,103–106] In such experiments, HGW is kept at the temperature of interest, and the crystallized fraction is tracked using Fourier-transformed infrared spectroscopy (FTIR)[10,105,106] or differential scanning calorimetry (DSC)[106] in experiments or using order parameters in simulations.[89,103,104]

The first ones to analyze the crystallization kinetics of HGW were Hage *et al.*[105] They deposited liquid $H_2O$ droplets mixed with small amounts of $D_2O$ on a window that was kept at 78 K. $D_2O$ at low concentrations allows for the observation of the decoupled OD stretching vibration, which is very sensitive to crystallization. Subsequently, they heated their samples to either 140, 144, or 146 K and followed crystallization by observing the time evolution of the OD stretching vibration. Their values for $n$ are shown in Fig. 7 (dark blue squares). Most of them are around 1.5 (within an error bar of 15%), which hints on either a constant nucleation rate and diffusion-controlled one-dimensional growth or no nucleation and three-dimensional diffusion-controlled growth.[107] Hage *et al.* interpreted their results in terms of the latter case, stating that ice I would grow as spherical particles, while nucleation is almost complete or negligible at these temperatures. An additional experiment that involves an annealing step slightly below the glass transition temperature of HGW prior to crystallization, however, shows a different behavior: The entire $f_{cryst}(t)$ curve can no longer be fitted with a single JMAK-fit, but requires the value of $n$ to change from initially 2.43 to 0.90. The initial value was interpreted as diffusion-controlled growth of spherical nuclei that had formed in the annealing step, while the second stage was attributed to the radial growth of cylindrical nuclei.

Later, they extended their studies to a larger set of temperatures and higher concentrations of $D_2O$[106] (light blue circles in Fig. 7). As one might suspect, the larger amount of $D_2O$ causes the kinetics to slow down and thereby decreases the rate constants while increasing the activation energy. In addition, Avrami exponents are lower compared to pure $H_2O$ at 150–155 K (see light blue circles in Fig. 7), indicating a pronounced isotope effect. For pure water, they added isothermal calorimetry experiments to measure the heat release during crystallization and thereby determine $f_{cryst}(t)$. The benefit of DSC over FTIR in this regard is that in FTIR, crystallites are only visible at a certain size, while DSC recognizes any kind of heat evolution. That includes the release/take-up of heat during strain-relief, nucleation, and microcrystalline growth. While the activation energies, and thereby also the rate constants, are similar for both DSC and FTIR, there are pronounced differences in Avrami exponents. These differences stem from heat evolution due to the above-mentioned effects, which can be seen in DSC but not in FTIR. Thus, they concluded that FTIR data are not suitable for an interpretation of $n$ that heavily relies on morphology.[106]

Another experimental investigation has been conducted by Maté *et al.* but employing a different hyperquenching setup.[10] They injected 2–3 bursts of liquid water droplets into a high-vacuum chamber through a pulsed valve, leading to an ~100 nm thick deposit. Additionally, they varied the deposition temperature between 14 and 90 K. Subsequently, they crystallized all samples

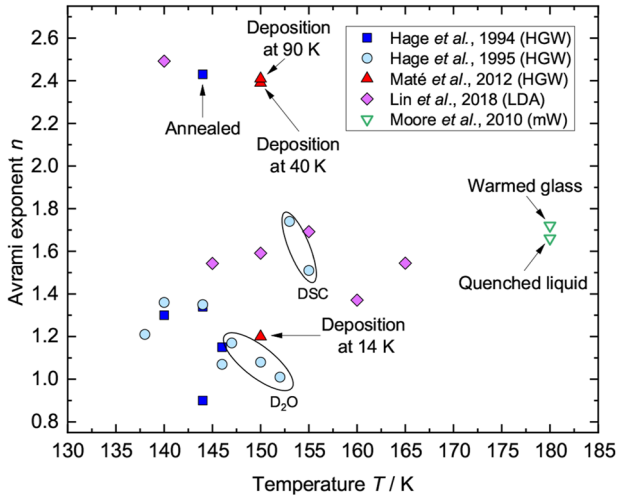


**FIG. 7.** Compilation of literature data for the Avrami exponent $n$ determined by isothermal crystallization experiments (filled symbols) of $H_2O$-HGW employing infrared spectroscopy[10,105,106] or calorimetry (data points inside ellipse marked DSC).[106] Additionally, the results of MD simulations (open triangles)[103] using the mW model and data on LDA[108] are shown. Data points in ellipse marked $D_2O$ are to identify work on $D_2O$.

isothermally at 150 K and measured $f_{cryst}(t)$ using FTIR, just as discussed above. Interestingly, their values for $n$ strongly depend on the deposition temperature (see Fig. 7), while $k$ barely changes. An increase from 14 to 40 K doubles $n$, but a further increase from 40 to 90 K leaves $n$ almost unchanged. The authors[10] interpreted these results as an indication of the existence of a structurally different form of amorphous ice at very low temperatures, which then would show altered crystallization kinetics. They ruled out that this pronounced jump in $n$ is caused by different initial morphologies since the same behavior is observed for ASW deposits. However, there are also other possible explanations. Hage *et al.* saw a comparable increase of $n$ only after annealing close to $T_{g,1}$ and concluded that nuclei that formed during that period serve as seeds for growth.[105] In light of that, it might also be possible that in the samples of Maté *et al.*, crystalline nuclei formed already during deposition at 40 and 90 K, but not at 14 K. Additionally, their heating rates to achieve 150 K are quite low (5 K $min^{-1}$), which means that partially nucleated samples will continue to nucleate even before the isothermal step commences, leading to $n > 2$. In the frame of this interpretation, the comparably low $n$ found after deposition at 14 K might reflect the lack of nuclei in that sample. In other words, only at that temperature, their setup would allow for a deposition with very few nuclei.

Another point we want to stress is that in the case of HGW, the JMAK-model seems to be only applicable to a limited degree. It has been shown that if the activation energy is time-dependent (other than usually assumed), the Avrami exponent can deviate significantly from the value one would expect based on the JMAK mechanism.[105] If the mechanism changes during crystallization, leading to a change of the activation energy and rate constant, the Avrami exponent might be misleading. Thus, for HGW, detailed

interpretations on the mechanism of crystallization should not rely only on the value of the Avrami exponent.

Computational studies related to the nucleation of ice in HGW are limited to several publications by Moore and Molinero.[89,103,104] Observing isothermal crystallization in MD-simulations requires large simulation boxes and comparably long time scales. Thus, such simulations are barely computationally feasible when employing atomistic water models. Therefore, these authors used a coarse-grained water model called monoatomic water (mW).[88] In this model, water is essentially represented as a single atom, but tetrahedral binding is encouraged through additional short-range interactions, which are supposed to mimic H-bonds. Upon cooling with less than 10 K $ns^{-1}$, it crystallizes at ~200 K, and upon slightly faster cooling, it exhibits a glass transition at ~150 K.[103] Thus, to study the crystallization kinetics, these authors chose 180 K, a temperature that sits between both limits. While they mainly focused on the crystallization of an "instantaneously quenched liquid" (QL), they also simulated the crystallization of a "warmed glass" (WG), which is essentially the computational equivalent of HGW prepared directly from the liquid. Interestingly, both materials (QL and WG) show similar crystallization kinetics as can be seen in the Avrami exponents shown in Fig. 7.[103] The slight difference between the two can be explained via different numbers of nuclei at the beginning of the crystallization. Other than that, their kinetic data agree quite well with the experiments of Hage *et al.* but not with those of Maté *et al.* Additionally, they carried out similar simulations at different temperatures and were able to determine a maximum in the crystallization rate of mW at around 200 K.[89] However, due to the faster dynamics of mW when compared to real water, this temperature might not be directly comparable to experiments. For this reason, they used literature data and classical nucleation theory to estimate a maximum at around 225 K.

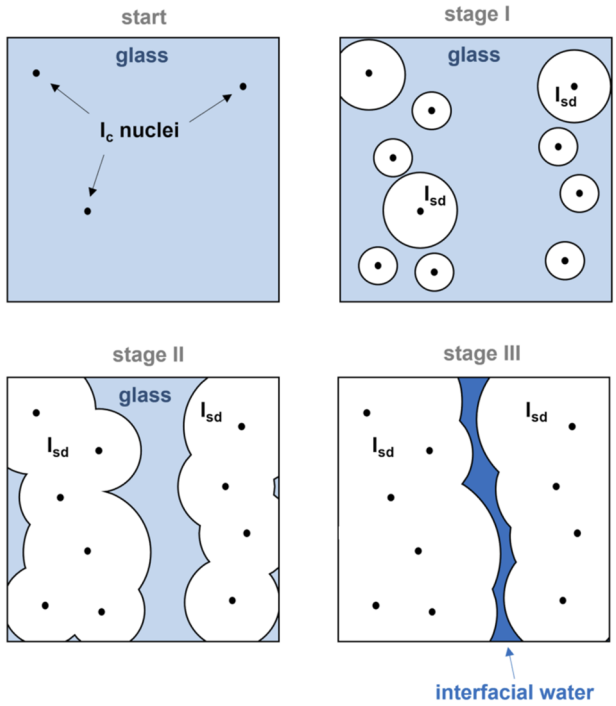


**FIG. 8.** Simplified schematic representation of the three stages of crystallization of a glass made from mW-water.[103,104] Start ($t$ = 0): Only a few nuclei that resemble cubic ice I ($I_c$) are present. Stage I: Nucleation and growth of stacking disordered ice I ($I_{sd}$). For simplification, these crystallites are represented in a spherical manner. In reality, they show a broad distribution of shapes. Stage II: Consolidation of the nuclei and crystallites. Stage III: Slow growth of large crystallites.

## B. Mechanism of crystallization in HGW

A major advantage of computational studies is the ability to directly gather microscopic data, which facilitate clarifying the mechanisms involved. The studies of Moore and Molinero[89,103,104] also shed light on the microscopic mechanism when crystallizing a warmed glass (WG). It is comprised of three different stages that are schematically shown in Fig. 8. Only a few nuclei are present in the beginning and the induction period is very short. Stage I commences during the first 40 ns in which the number and size of nuclei increase rapidly. The size of the critical nuclei is approximately ten water molecules. The initial structure of the nuclei resembles cubic ice I ($I_c$). However, when the nuclei grow, hexagonal ice I ($I_h$) layers grow on top of the cubic nuclei. Therefore, hexagonal stacking faults are already present at stage I. Thus, stage I can be classified as nucleation and growth of stacking disordered ice I ($I_{sd}$).[104]

Between 40 and 100 ns of simulation time, the number density of nuclei increases more slowly until it reaches a maximum. After 100 ns, the number density of nuclei decreases, which indicates stage II, namely, the consolidation of nuclei and crystallites.[104] Several processes were identified: (i) direct attachment, (ii) rearrangement, and (iii) non-consolidation. Direct attachment (i) occurs when two crystallites have parallel stacking axes and grow toward each other. Once they are close enough, they just merge into a single crystallite. Rearrangement (ii) is observed when the stacking axes are misaligned. This causes in most cases a rearrangement of the smaller crystallite to align said axes again to perform direct attachment. In case both crystallites are too large for rearrangement, non-consolidation (iii) occurs. In this case, the crystallites do not merge and are separated by layers of interfacial ice and liquid water. Stage III involves a slow growth of the crystallites without change in their number density. Crystallization is finished once no crystallites can be consolidated anymore in the accessible time scales, which is the case after 590 ns.[104]

While it is conceivable that similar kinds of mechanisms may also take place in real samples of HGW, there are some differences that are not accounted for in simulations. The most notable one is the presence of individual droplets and interfaces between droplets already in the vitrified state. Figure 9 shows an electron microscopy image of HGW samples after shading with metals. Individual droplets and interfaces between them are clearly visible. That is, there are interfaces between individual droplets, which produce a significant level of strain between individual droplets. It is entirely unclear whether nucleation in such HGW samples takes place at these interfaces or within the bulk of individual droplets. In addition, the question whether or not the strain levels are reduced and whether these interfaces disappear above the glass transition, possibly even prior to crystallization, has not been clarified yet. Nonetheless,

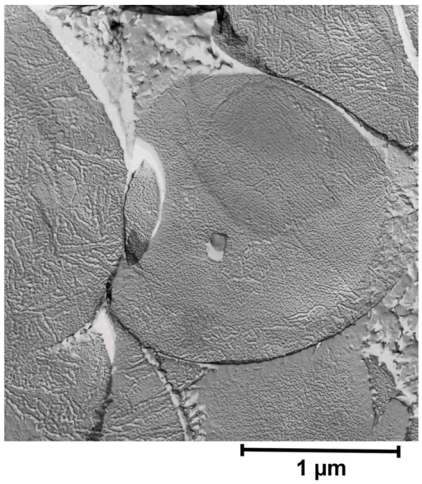


**FIG. 9.** Ultrastructure of the vitrified HGW sample at 80 K as observed in the electron microscope after shading with platinum. The droplet diameter seen after splat-cooling (i.e., hyperquenching) is typically ~2 to 3 $\mu$m. Cut through the glassy sample is approximately parallel to the incident beam of water droplets of an initial diameter of ~3 $\mu$m in the liquid state. Note the well-defined interfaces between individual droplets and fractures.

there is good agreement between experimental[105,106] and computational[103] Avrami exponents, suggesting similar mechanisms during crystallization of HGW. That said, the previous discussion of the mechanism of crystallization might also be valid for the experiment and might point into the direction that droplet coalescence takes place in the experiment prior to crystallization. Such kind of droplet coalescence would, furthermore, indicate that the HGW sample turns into an ultraviscous liquid above its glass transition temperature (near 136 K).[99] Apparently, a question of such importance needs more proof than just similar Avrami exponents. Direct experiments related to the dynamics of the interfaces are desirable. From the experimental point of view, the details of how preparation history and crystallization temperature influence the Avrami exponent are still unclear. The experimental studies mentioned here focus on using FTIR, where the downsides of this method have already been mentioned above. More calorimetric studies that systematically probe the effect of different deposition-, annealing-, and crystallization-temperatures could help to answer open questions. On the simulation side, it would be desirable to assess how robust the mechanisms are upon the change of the water model, e.g., when going from the coarse-grained mW model to atomistic models, such as TIP4P/ice or the like.

## IV. NUCLEATION AND GROWTH IN AMORPHOUS ICE AT PRESSURES UP TO 2 GPa

### A. Polyamorphism

Amorphous ice can also be produced via pressure-induced amorphization (PIA) at low temperatures. Three distinct amorphous ices are distinguished based on their density and local coordination of water molecules. ASW and HGW discussed so far both belong to the LDA family of amorphous ices. Amorphous ices of higher density in the high-density amorphous (HDA) and very-high-density amorphous (VHDA) ice families are usually produced starting from hexagonal ice. Pressurization of ice $I_h$ beyond 1.2 GPa at 77 K is the most-widely used method and the historically first method developed by Mishima *et al.*[14] Upon compression at low temperatures, ice $I_h$ amorphizes first into what is called at the present time unannealed HDA (uHDA) to distinguish from more advanced preparations. This nomenclature was brought forward by Nelmes *et al.*[109] and Winkel *et al.*[110] in their work on pressure-annealing of uHDA. At temperatures above 77 K, uHDA slowly progresses toward an equilibrium form, where three different equilibrated end states are known. In the pressure range below about 0.2 GPa, LDA is the equilibrated amorphous ice; between 0.2 and 0.8 GPa, it is HDA; and between 0.8 and 3 GPa, it is VHDA.[3] Annealing above 0.8 GPa induces a transformation of uHDA into more dense VHDA, while at lower pressures, a relaxation to the lesser dense "expanded HDA (eHDA)" is observed. This eHDA form represents a more relaxed and homogeneous form of HDA that is closely related to the high-density liquid state HDL, by contrast to uHDA, which still contains distorted, crystalline remnants.[111–114] The key characteristic of these processes upon annealing is that they bring the amorphous ice closer to the metastable equilibrium. For this reason, they are inevitably irreversible relaxation processes. uHDA never reappears through changes of pressure because of its unstable, high-energy nature, whereas eHDA or VHDA can be made through different routes and represent metastable equilibrium states. For instance, eHDA is obtained both upon heating uHDA at 0.2 GPa to 140 K and upon decompression of VHDA to 0.2 GPa at 140 K.[110] Such equilibrated amorphous ices can be kept (meta)stably for many years without significant changes in their (thermodynamic) properties, such as excess entropy or excess volume. For this reason, they are quite similar to stable ice phases, but there is always a crystalline ice phase that is thermodynamically more stable than the equilibrated amorphous ice. Furthermore, these three amorphous ices experience amorphous-to-amorphous phase transitions upon changing pressure and/or temperature, a phenomenon that very much resembles the behavior of thermodynamically stable crystalline phases of ice. The phase transitions between these amorphous ices are sharp and jump-like, e.g., the density changes suddenly by about 25% at the HDA-to-LDA transition, where LDA nuclei form within the HDA-matrix and grow at their expense. The transition can then also be reversed, with some hysteresis, by changing the pressure. Such behavior is quite atypical for amorphous or glassy materials and has been termed "polyamorphism." The idea behind polyamorphism is that such equilibrated amorphous ices represent proxies of equilibrium liquids, with the only difference that structural relaxation times are above 100 s in amorphous ices, but below 100 s in deeply supercooled liquids. The temperature at which the criterion distinguishing the amorphous solid and the deeply supercooled liquid is reached is called the glass transition temperature $T_g$. Three distinct glass transition temperatures for the three distinct amorphous ices have been reported experimentally and mapped as a function of pressure.[27] There is an ongoing debate and scientific work yet to be done to settle the issue whether or not the amorphous ices, indeed, turn into liquids above their respective $T_g$s. Recent evidence seems to affirm the thermodynamic continuous connection of HDA and LDA with the supercooled liquid, whereas for VHDA, some more research is required to answer the question.[115] It has been suggested

by Stern *et al.* that amorphous ices crystallize before they can reach the deeply supercooled liquid state above 0.3 GPa, but turn into the liquid before crystallizing below 0.3 GPa.[31]

This question whether or not crystallization takes place from the amorphous solid or from the deeply supercooled liquid is key when interpreting measured crystallization rates. One important idea to keep in mind is that pre-existing ice nuclei may remain in the amorphous solid, but disappear at the transition into the deeply supercooled liquid. While uHDA is understood to contain such pre-existing nuclei, eHDA contains much less of them, or even none. These nuclei may even survive the amorphous–amorphous transition from HDA to LDA. That is, uHDA or eHDA decompressed at lower temperatures leads to LDA-I and LDA-II, respectively, where LDA-II is more homogeneous and closer to its metastable equilibrium,[116] while uHDA and, subsequently, LDA-I show nanocrystalline remnants in the amorphous matrix.[113]

Besides PIA, other methods have also been employed to amorphize ice polymorphs: Upon isobaric heating of $I_h$ from 77 K to 155–170 K at pressures between 0.50 and 1.00 GPa, temperature-induced amorphization occurs.[117] Isobaric heating above 120 K of recovered ice VIII or VII at ambient pressures also yields LDA.[118–122] Another unusual route to LDA is rapid decompression of ice VIII from pressures above 5 GPa to vacuum at temperatures between 140 and 165 K.[108] Rapid decompression of ice VIII at low temperatures results in a transition to ice VII, which then upon slow heating amorphizes into HDA at 86 K and turns to LDA above 107 K.[123]

The crystallization behavior of these amorphous ices is highly case-dependent, very much affected by the specific route to make it, the pressure, and the heating rate during annealing. These factors determine not only the form of crystalline ice it transforms into but also the onset temperature and kinetics of crystallization. In addition, the question whether or not the amorphous matrix carries crystalline remnants has a tremendous impact on the combined rate of nucleation and growth of such amorphous ices. Obviously, amorphous ices carrying less crystalline remnants crystallize most slowly and can be heated to higher temperatures before they crystallize. That is, high crystallization temperatures $T_x$ prove the high quality of the pure amorphous samples, whereas low crystallization temperatures imply preparation routes that lead to non-homogeneous amorphous ices, i.e., amorphous ices with crystalline remnants. These crystallites are too small to show long-range order. For short-range order, studies of molecular structure can give insights into similarities between distorted nanocrystals in the amorphous matrix and crystalline ice phases: X-ray diffractograms of LDA and ice I indicate similarities in density and structure (Ref. 124 and references therein). Raman spectra of HDA and VHDA show similarities to ice VI (Ref. 124 and references therein). However, the resulting crystalline phase into which an amorphous ice with nanocrystalline remnants crystallizes provides more conclusive evidence about the structure of nanocrystals. uHDA still contains distorted, crystalline ice $I_h$ remnants, the result of an incomplete amorphization of ice $I_h$ at low temperature.[111] Upon heating at pressures between 0.25 and 0.50 GPa, these ice $I_h$ nanocrystals in uHDA transform to ice IX seeds.[112,113] Similarly, eHDA that had been annealed below 0.2 GPa shows the presence of LDA seeds, which turn to IX nanocrystals upon heating above 0.17 GPa.[113] During transformation of uHDA to LDA-I upon heating at pressures as low as 0.001 GPa, ice $I_h$ seeds are preserved within the amorphous matrix.[111]

### B. Crystallization of amorphous ices at different pressures

Starting at vacuum[108] to low pressures below 0.1 GPa,[113,125] non-LDA types of amorphous ices first undergo polyamorphic transitions in a step-like manner to the respective form of lower density until LDA is reached, e.g., VHDA transforms upon heating first to HDA, which then turns to LDA. After a glass-transition to low-density liquid (LDL),[108] crystallization to stacking disordered ice $I_{sd}$ takes place. [Although the literature frequently speaks of cubic ice $I_c$, full cubicity is hardly reached (Ref. 126 and references therein) in these experiments, so the reader is reminded that $I_c$ is frequently used synonymously for hexagonal-cubic stacking disordered ice $I_{sd}$.] In this Review, we only cover nucleation and growth of crystalline ices even though nucleation and growth processes have also been identified for the polyamorphic transition producing LDA/LDL.[127] That is, the polyamorphic transition involves nucleation of amorphous ice in an amorphous matrix,[113,114] interfaces between amorphous ices of different densities, and growth of domains. This new kind of physics at the heart of the polyamorphic transition has not been investigated quantitatively, though, so far.

Only LDA-I, deriving from (unannealed) uHDA, does not crystallize into a single ice phase, but instead, a mixture of $I_{sd}$ and hexagonal ice ($I_h$) forms. This likely derives from two crystallization channels: one from the LDA-matrix and the other from hexagonal remnants in uHDA, preserved even after decompression to LDA-I.[111,128]

The crystallization product of HDA changes with the increasing pressure, starting with $I_{sd}$ at low pressures, continuing to ice IX,[129] ice V,[130] ice IV,[131] and ice XII[132] and ending with ice VI[133] at 2 GPa. This is schematically depicted in Fig. 10(a). Between 0.1 and 0.3 GPa, crystallization is preceded by a glass transition to supercooled high-density liquid (HDL) water. At higher pressures, the timescales for crystallization decreases significantly in relations to relaxation, so crystallization occurs directly from the amorphous solid state.[31]

Salzmann *et al.*[134] found that at pressures of 0.21–1.41 GPa, crystallization shows characteristics of parallel reactions to two or even more ice phases. They observed the simultaneous formation of ices $I_{sd}$ and IX at 0.21 GPa; ices $I_{sd}$, IX, and V at 0.31 GPa; ices IX and V at 0.51 GPa; ices IV, V, IX, and XII at 0.71 GPa; ices IV and XII at 0.81 and 1.21 GPa; and ices XII and VI at 1.41 GPa. At pressures of at least 1.91 GPa, only ice VI forms. When deriving from uHDA, at low pressure ice IX, formation is contaminated by ice $I_h$ crystallization. Similarly to the crystallization behavior of LDA-I, hexagonal nucleation sites of uHDA cause the formation of a mixture of ice $I_h$ and ice IX.[111]

The description of eHDA's crystallization behavior applies just to VHDA as well. This is because over the pressure range, the equilibrated amorphous phase changes continuously from HDA to VHDA. Annealing VHDA at pressures below roughly 0.8 GPa induces a transition to eHDA, and annealing of HDA at pressures above results in a transition to VHDA, before crystallization sets in Refs. 31 and 135. However, the annealing temperature of VHDA is of importance and determines the absence of nanocrystalline remnants.[31]

The onset temperature of crystallization $T_x$ behaves across the discussed pressure range just as complex: It depends on multiple factors, which include pressure, heating rate, preparation route, and

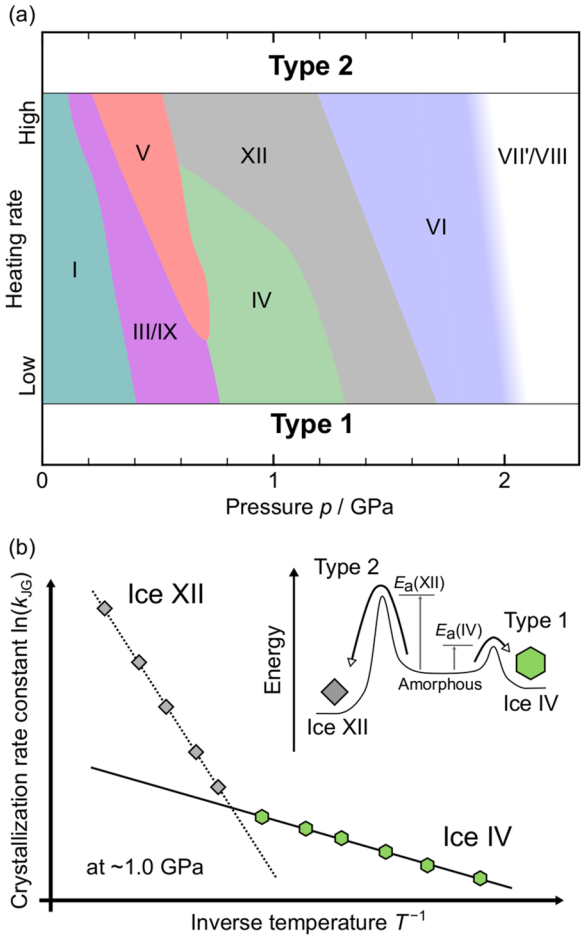


**FIG. 10.** (a) Schematic diagram of pressure-dependence of crystallization kinetics for crystalline ice phases from experimental observations.[134] The diagram indicates which ice polymorph crystallizes preferentially at the given pressure and heating rate from amorphous ice. Typically, a mixture of two ice polymorphs crystallizes in parallel, where type 1 crystallization is favored in slow heating experiments, but type 2 for fast heating. (b) Schematic illustration of the temperature dependences of logarithmic crystallization rate constant ($k_{JG}$) for types 1 and 2. Crystalline phases of ice IV (type 1) and XII (type 2) at ~1 GPa are taken as an example. The inset shows a schematic energy landscape, indicating the different activation energies ($E_a$) for the two types of crystallization.

density of the amorphous state. The crystallization shifts to higher temperatures with the increasing pressure, starting with temperatures close to 140 K at atmospheric pressure and reaching as far as 184 K at 1.8 GPa. However, this "boundary to no man's land" takes after 1.8 GPa a sharp turn, i.e., $T_x$ decreases with $p$ for $p > 1.8$ GPa, as seen in Fig. 11. In fact, at pressures above 4 GPa, amorphous ice is no longer stable and crystallizes upon compression even at temperatures below 100 K.[136] Thus, by choosing higher heating rates, long crystallization times can be overcome at low temperatures and crystallization sets in at higher temperatures. For this reason, a comparison of $T_x$ is only meaningful for the same heating rates.[134]

$T_x$ is also influenced by the amount of nanocrystalline remnants in the amorphous matrix as crystallization is catalyzed at these nucleation sites. This is why uHDA and LDA-I tend to crystallize at significantly lower temperatures than eHDA and LDA-II, respectively. For VHDA, the pressure of annealing is of importance. While annealing pressures of 1.1 GPa are not sufficient to eradicate crystalline remnants completely, after annealing at 1.9 GPa, a form of VHDA is formed, which exhibits the highest $T_x$. Interestingly, for eHDA, a higher annealing pressure shows no effect on $T_x$. It remains unclear whether no seeds are present in both types of eHDA at the end of decompression or new seeds are introduced during decompression for both.[135] However, it is critical to which pressure eHDA is decompressed to: Decompression of eHDA to pressures below 0.2 GPa causes a significantly lower $T_x$ for heating at pressures above 0.17 GPa than decompression to 0.2 or 0.3 GPa. This is because during decompression to low pressures, nanodomains of LDA form, which then transform into ice IX nuclei upon heating.[113]

Comparing VHDA and eHDA, which have both been annealed at 1.9 GPa, shows the effect of the density on $T_x$: VHDA exhibits the highest $T_x$ and, thus, can be used to map the low-temperature boundary to water's no man's land[31] in Fig. 11. Only at pressures of up to 0.3 GPa, both eHDA and VHDA crystallize at almost the same temperature. Stern *et al.* argued that this effect is a result of the preceding glass transition to high-density liquid (HDL), where both eHDA and VHDA turn into the same metastable high-density liquid, which then crystallizes.[135]

### C. Crystallization rates of LDA

The number of kinetic studies on LDA crystallization is limited, especially concerning LDA synthetized involving pressure-induced amorphization. This is due to its structural similarity to HGW and especially ASW. Quite often, ASW, HGW, and LDA are used synonymously in the literature,[137] where most studies in the literature pertain to ASW (see paragraphs above). In the case of LDA, there have been some studies that were done *ex situ*, in contrast to ASW and HGW. Crystallization of LDA was monitored using ultrafast laser methods so that temperatures as high as 200 K and above could be studied.[126,138] Furthermore, slow heating experiments did probe the crystallization kinetics at temperatures below 170 K.[108] The crystallization kinetics of the low-density liquid form synthetized by rapid decompression of ice VIII at temperatures between 140 and 165 K had been investigated by Lin *et al.*[108] Using time-resolved x-ray diffraction, they were able to monitor *in situ* structural changes within milliseconds at isothermal and isobaric conditions. The Avrami exponent for the observed crystallizations between 145 and 165 K is ~1.5, indicating a diffusion-controlled growth of spherical nuclei.[107,108] At 140 K, the Avrami exponent diverts from this trend and lies close to 2.5, which would imply diffusion-controlled three-dimensional growth.[107] This might be linked to the relatively long nucleation duration at 140 K. Avrami exponents are included in Fig. 7.

For a direct comparison, we calculated from the Avrami exponent $n$ and the crystallization time $\tau$, the crystallization rate constant $k_{JG}$; Fig. 12 shows collected rate constants at 150 K plotted against the pressure for comparison.

In their studies, Lin *et al.* reported $k_{JG}$ at each temperature and noted an increase in the slope above 155 K. They offered possible explanations for this increase in crystallization kinetics. They argued

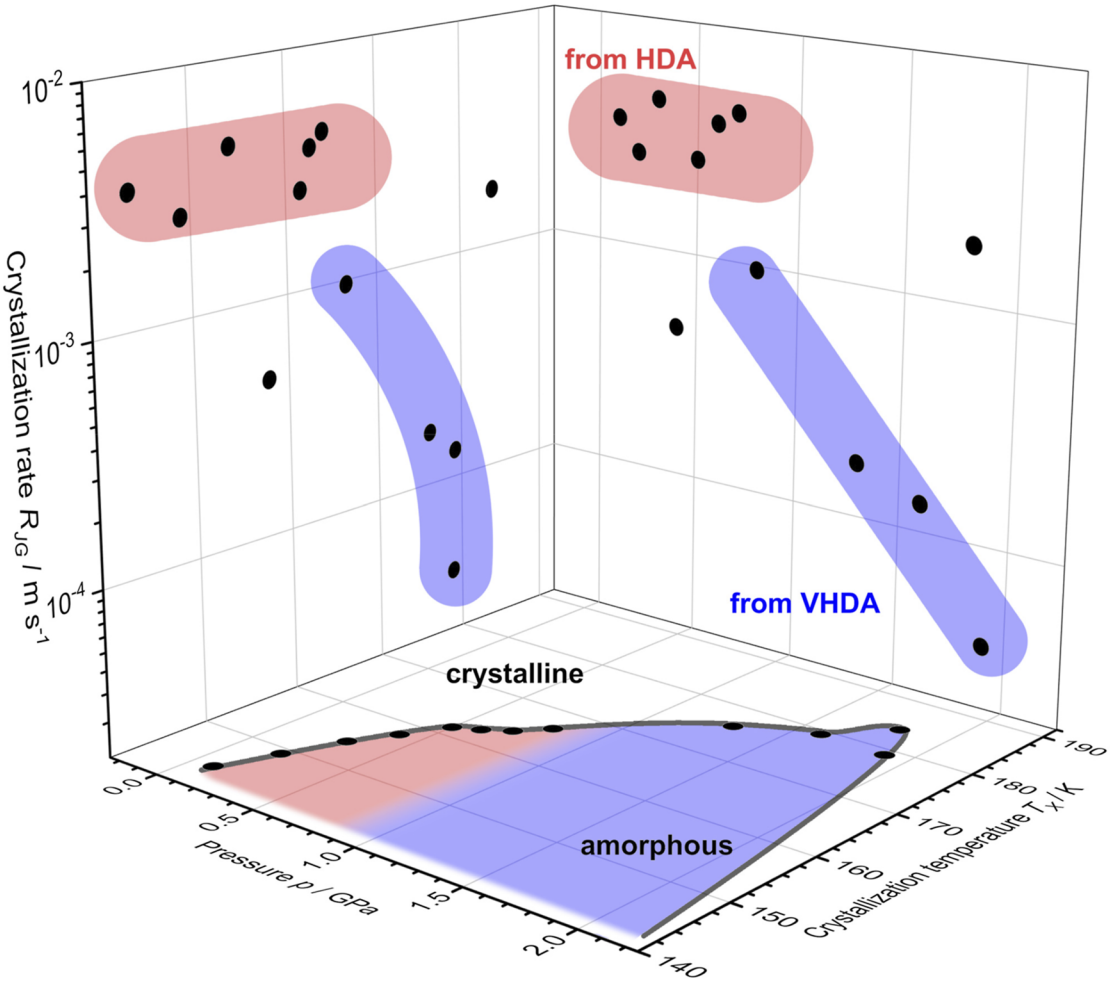


**FIG. 11.** Relation between pressure $p$, crystallization temperature $T_x$, and rate of crystallization $R_{JG}$ for HDA and VHDA. Data taken from Ref. 136 and from Ref. 31, where the uniaxial growth rates are obtained by division, using the bore cross section of the piston cylinder cell (~50 mm$^2$). Trends are indicated in color as a guide to the eye. The change from red to blue near ~0.8 GPa marks the transition from HDA to VHDA. Note that LDA between 0.0 and 0.1 GPa is not shown in the diagram for simplification. Therefore, the jump-like change HDA to LDA [with $T_x$(LDA) ≈ 150 K] is missing.

that it might be linked to a decoupling of self-diffusion from structural relaxation, which has been observed in metallic glasses close to the glass-transition temperature (Ref. 108 and references therein). Another possibility they pointed out is a fragile-strong dynamic crossover (Ref. 108 and references therein).

However, their temperature region was limited up to 165 K by the time resolution (at a few milliseconds) in x-ray diffraction measurements at that time. The first and second halo peaks of the non-crystalline states typical of LDA, but distinct from liquid water over 230 K,[139,140] suggest the tetrahedrally coordinated network developed in LDL. For the temperature range of 165–200 K, kinetic studies have recently been provided by Kim *et al.*[138] and Ladd-Parada *et al.*[126] Their studies on crystallization of amorphous ice at ambient pressures upon ultrafast heating involve a temperature-jump of 90 and 60 K in 20 ps to 205 and 200 K induced by a 100 fs IR pulse in eHDA and LDA samples, respectively. By using time-resolved wide-angle x-ray scattering, crystallization was monitored in the early stages at time scales of 10–1000 $\mu$s.

Both Kim *et al.*[138] and Ladd-Parada *et al.*[126] then fitted their data to the JMAK model, assuming an Avrami exponent of 4 and implying constant nucleation rates and three-dimensional interface controlled growth.[107] Furthermore, they suggested a HDL to LDL conversion before crystallization and used for the nucleation rate a fixed value from the study of Kimmel *et al.* on transiently heated ASW films.[62] Yet, they declared the determined growth rates to be directly connected to LDA and eHDA. Kim *et al.* compared time scales of the LDL domain growth between 20 ns and 3 $\mu$s to consecutive crystal growth time scales of 3–50 $\mu$s, which they used to support their findings of a liquid–liquid transition.[138]

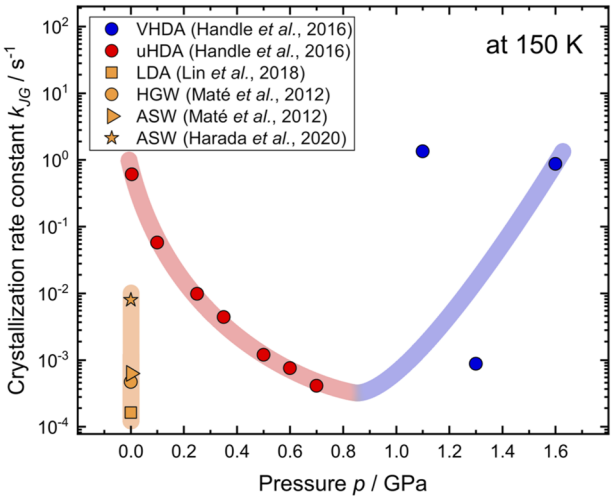


**FIG. 12.** Crystallization rate constants $k_{JG}$ at 150 K against $p$. A color-coded guide to the eye illustrates the trend: LDA-like samples in orange (LDA,[108] ASW,[10,63] and HGW[64]), HDA-samples in red, and VHDA-samples in blue.[135] Note the jump-like change from LDA to HDA and the dynamics minimum between HDA and VHDA near 0.8 GPa, which is linked with a jump in $T_g$ and viscosity.

### D. Crystallization rates of HDA/VHDA up to 2 GPa

Regarding the crystallization kinetics of HDA and VHDA, the crystallization has to be discussed with respect to the pressure. For this, we try to give an overview of the crystallization behavior for pressures of up to 2 GPa.

In an aim to qualitatively describe the complex crystallization behavior of HDA to multiple ice phases, Salzmann *et al.*[134] investigated the kinetics of crystallization at pressures between 0.2 and 1.9 GPa at different heating rates. They identified two different types of crystallization kinetics, called type 1 and type 2. In type 1 crystallization, the ice polymorph grows slowly at low temperatures, whereas for type 2 crystallization, rapid growth at higher temperature is observed. Consequently, the relative yield of each ice phase is controlled by adjusting the heating rate. The kinetics of these parallel reactions can be visualized by comparing the temperature dependence of the $k_{JG}$ of types 1 and 2 in Fig. 10(b) in the linearized form of the Arrhenius equation,

$$\ln(k_{JG}) = \ln(A) - \frac{E_a}{R}\frac{1}{T}. \quad (4)$$

Type 1 slow kinetics at low temperatures, which are suppressed at higher temperatures, are linked to a low preexponential factor $A(1)$ and a low activation energy $E_a(1)$ and vice versa for type 2 kinetics. These kinetics are illustrated in Fig. 10(b) on the example of competitive ice XII and IV crystallization. These type 1–type 2 pairs are ice $I_h$ and ice IX at 0.21 GPa, ice IX and ice V at 0.51 GPa, ice IV and ice XII at 0.81 and 1.21 GPa, and ice XII and ice VI at 1.41 GPa. Only at 0.71 GPa, this behavior showed to be even more complex, with four parallel crystallizations to ices IX, V, IV, and XII occurring. For these, they assigned ice IX and XII to type 1 and 2 kinetics, respectively, and ice V and IV to have kinetics in between. Figure 10(a) shows a visualization of these crystallization products with respect to the pressure. Upon a pressure increase, type 1 crystallization is suppressed, while type 2 crystallization kinetics significantly slows down. This mirrors type 1 kinetics, and an added crystallization to an ice phase of higher density then shows type 2 behavior.

Handle and Loerting[135] fitted volumetric changes upon isobaric heating of eHDA and VHDA at pressures between 0.004 and 0.70 GPa and between 1.1 and 1.6 GPa to estimate crystallization rate constants $k_{JG}$. These transformations were investigated and characterized by *in situ* volumetry, *ex situ* XRD and DSC measurements. While at pressures of 0.2–0.7 GPa, VHDA transforms into eHDA, at pressures above 1.1 GPa, eHDA turns to VHDA. After this relaxation, first a glass transition and then crystallization take place from the respective metastable "equilibrated state."

The rate of crystallization $k_{JG}$ as a function of temperature was determined at each pressure by fitting their dilatometric data.[135] They found that from 0.1 to 0.7 GPa, $k_{JG}$ decreases with pressure and increases again at pressures above at least 1.1 GPa. They regarded the minimum near 0.8 GPa to be a dynamic anomaly that is closely related to the HDA/VHDA transition taking place. The respective $k_{JG}$ at 150 K has been calculated for this Review and plotted against pressure to compare with LDA,[108] ASW,[10,63] and HGW[10] in Fig. 12. The crystallization rates observed by Handle and Loerting[135] in Fig. 12 are, in general, much higher than the ones observed by Stern *et al.*[31] shown in Fig. 11. This indicates that the number of crystal nuclei is much larger in the study by Handle and Loerting. The absence of such nuclei suppresses crystallization in the study by Stern *et al.* very much, especially for VHDA, where the pressure dependence changes between the two studies. Commonly, both studies observe a significant and rapid change at 0.8 GPa, which was called the dynamic anomaly. This anomaly is caused by the underlying HDA/VHDA transition, which takes place in a narrow pressure interval close to 0.8 GPa. Both of these studies were carried out in the Innsbruck lab, and the results again underline how important preparation paths and nuclei are for enhancing or suppressing crystallization rates.

Simultaneously, the glass transition shows an inverse effect, increasing to 0.7 GPa and then dropping again upon further pressure increase. The correlation between these two behaviors can be explained by the link between a higher $T_g$ and an increased viscosity at the time of crystallization, consequently hindering crystallization. The increase in $k_{JG}$ above 1.1 GPa is linked to a continuous HDA-to-VHDA transition and faster hydrogen bond dynamics in VHDA.[135]

Stern *et al.*[31] did a comprehensive study on crystallization temperatures and times upon heating with 2 K min$^{-1}$. They defined the crystallization time as the time that passes between crystallization onset and end temperature, which is monitored via volumetric changes during isobaric experiments. They found that below 0.3 GPa, both eHDA and VHDA share the same crystallization temperature and rate. This has been attributed to the fact that at these pressures, both reach the same state, namely, HDL, before crystallization.

Figure 11 summarizes crystallization times and temperatures of VHDA at different pressures obtained by Stern *et al.* and shows some interesting trends. Counterintuitively, even though the crystallization temperature increases with pressure rise, the crystallization

rate decreases. This is attributed to the higher viscosity and, consequently, higher self-diffusivity at lower pressures. With the drop of crystallization temperature at 1.9 GPa, the kinetics slow down even further with a change of slope. Observing the crystallization rate against the pressure, the drop in the crystallization rate around 0.8 GPa is most evident. This is due to VHDA being progressively more stable in relations to HDA, which slows down crystallization immensely.

## V. NUCLEATION AND GROWTH IN AMORPHOUS ICE AT PRESSURES ABOVE 2 GPa

### A. Crystallization of (V)HDA into ice VII′

While (V)HDA remains in the non-crystalline form over 100 K at pressures of up to 2 GPa, amorphous ice can crystallize even at 77 K by compression to 4 GPa into the so-called base-centered-cubic (b.c.c.) ice, with a b.c.c. oxygen sublattice.[136] The uniqueness of this b.c.c. ice is described in the later paragraphs. While reported crystallization temperatures and pressures contain large uncertainties for the technical difficulties of pressure-temperature control, there is an overall trend in which VHDA crystallizes at lower temperatures upon an increase in a pressure regime over 2 GPa[124,130,136,141–143] in contrast to the pressure regime below 1.8 GPa (see Figs. 11 and 13). The crystallization behaviors of (V)HDA are also very much affected by experimental procedures. Apart from the crystallization itself, it is still ambiguous whether the amorphous ice can be regarded as still HDA or sufficiently transformed into VHDA before the crystallization. An example of an exception, (V)HDA compressed by the back-and-forth approach can remain up to 5.5 GPa at 100 K (point A in Fig. 13).[124] On the other hand, amorphous ice obtained by decompression of b.c.c. ice re-crystallizes at lower pressure in the second compression (2.2 GPa at 135 K; point B in Fig. 13) than that in the first compression starting from ice $I_h$ (3.3 GPa at 135 K; point B′ in Fig. 13).[142] The negative relation between the crystallization pressures and temperatures can be attributed to the similarity of the local oxygen arrangements between the HDA and b.c.c. ice, revealed by the total scattering experiments at 2.2 GPa.[141] At higher pressures, local structures of HDA get closer to those of the b.c.c. ice, which can result in smaller activation barriers for crystallization.

In contrast to the parallel crystallization below 2 GPa, HDA only crystallizes into the b.c.c. ice above 2 GPa. In the high-pressure regime above 2 GPa, the thermodynamically stable crystalline phases are ices VII and VIII. Their hydrogen-bond networks have identical oxygen sublattices, but different alignments of molecular orientations: molecular orientations are ordered in ice VIII, while those are randomly disordered in ice VII. Their ordering transition proceeds so fast that ice VII cannot remain in the disordered form but completely transforms into ice VIII upon cooling below 274 K at 2–10 GPa. Despite the crystallization of HDA occurring in the stable region of ice VIII, the crystallized ice is almost identical to ice VII except for weak features evidencing some degree of order. Hence, this crystallized ice can be regarded as a partially ordered ice VII and is called ice VII′,[136] where the prime (′) distinguishes it from ice VII. It should be noted that the interim notation with prime is also used for ice VII in other states, such as in its dynamically disordered form at high temperatures and pressures.[146] Hereafter, ice VII′ in this Review indicates the b.c.c. ice crystallized from amorphous ice. Molecular orientations in HDA are in a non-equilibrium distribution, i.e., mostly disordered, where some orientational correlations may persist after crystallization, producing not a fully, but partially disordered ice. When HDA is crystallized at a high temperature of ~160 K and 2.6 GPa or when ice VII′ is heated, the thermodynamically stable ice VIII form is accessed.[136] This is because at higher temperatures, molecular reorientations are unlocked.

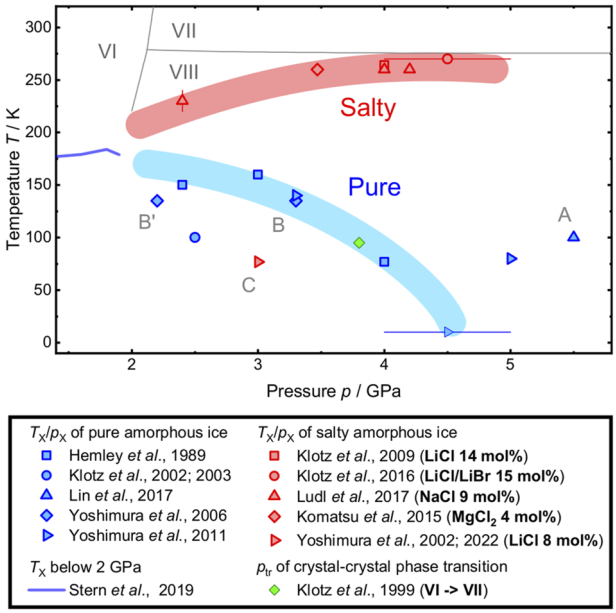


**FIG. 13.** (V)HDA crystallization temperature ($T_x$) upon heating and crystallization pressure ($p_x$) upon compression, resulting in ice VII′. For orientation, the ice VI/VII/VIII triple point is indicated. Blue and red symbols represent the studies of pure ice and salt-bearing ice, respectively. Shaded lines are guides to the eye. The blue line below 2 GPa is taken from Ref. 31 (same as Fig. 11). The green diamond indicates the crystal–crystal transition from ice VI to ice VII by compression. Points A, B, B′, and C mark exceptional results for the back-and-forth compression,[124] second compression starting from ice $I_h$,[142] first compression starting from LDA prepared by decompression of ice VII′,[142] and salt-bearing ice starting from a non-vitrified crystalline state,[144,145] respectively.

Metastable ice VII retaining the disorder of molecular orientations at low temperatures can also be produced from ice VI by compression at 95 K.[119] However, this ice VII does not show any features of hydrogen ordering in contrast to ice VII′ crystallized from amorphous ice at similar $pT$ conditions (Fig. 13)[130] and other ice phases II, III/IX. These can be related to the mechanism of solid–solid transitions with an intermediate non-crystalline state.[108,147] The actual mechanism and their relations are not clear, but involve rearrangements of molecular orientations accompanied by oxygen-sublattice rearrangements.

The relation between the liquid and amorphous states is a fundamental question as outlined in this Review and seen in the long-standing scientific discourse about the liquid–liquid critical point (LLCP) model.[148] Crystallization behaviors can provide an idea from a different perspective. In rapid compression using dynamic diamond anvil cells (DACs),[149,150] liquid water can remain in a non-crystalline state metastably up to 1.8 GPa followed by direct

crystallization into ice VII rather than thermodynamically stable ice VI. Such kinetic preference is ascribed to the lower interfacial energy between ice VII and liquid (23 ± 1.9 mJ $m^{-2}$) than that between ice VI and liquid (29 ± 0.9 mJ $m^{-2}$), implying the similarity of their local molecular arrangements as well as the case of ice VII′ crystallizing from amorphous ice at low temperatures. Hence, the supercompressed high-density liquid can be connected to high-density amorphous ice for their crystallization behavior from non-crystalline states to b.c.c. ice.

### B. Salty ice VII from glassy saline solution

The HDA/ice VII′ crystallization also shows interesting behavior in the presence of ionic species. When starting from vitrified saline solutions containing 14 mol. % of LiCl, amorphous ice persists in the non-crystalline form up to 271 K, slightly lower than the phase transition temperature of ice VII–VIII (~274 K at 2–10 GPa) upon heating at 4 GPa.[151] The onset temperature of crystallization is around 264 K. By contrast, pure water amorphous ice never persists above 190 K (see Fig. 11). Other experiments using different ionic species (LiBr,[152] NaCl,[153] and $MgCl_2$[154]) also resulted in similar persistence of the amorphous phase (Fig. 13). The existence of ionic species can hinder molecular reorientations in ice[151,155,156] and can increase the activation energy of the crystallization with concerted molecular rearrangements. Here, questions about how ionic species behave during crystallization arise. One question is the place where the crystallization initiates, in other words, whether ionic species enhance or inhibit the nucleation. The next question is what factor dominates the bulk crystallization of salty ice VII′. The last one is whether crystallization of salty ice VII′ occurs congruently, i.e., without bulk segregation of ionic species. These are related to both local and global structural changes, including molecular reorientations and ion diffusion. While it is still unclear how the incorporated ionic species affect the crystallization of amorphous ice, they appear to enlarge the stability region of saline amorphous ice.

Despite the consistent elevation of $T_x$ for most saline amorphous ice in diffraction studies,[151–154] there is an exception from Raman measurements, which reports crystallization of LiCl-bearing amorphous ice at 3 GPa and 77 K (point C in Fig. 13).[144,145] This experiment started with PIA of crystalline ice I, while the other diffraction studies started from amorphous ice directly vitrified from a highly concentrated liquid solution,[151,152] with cooling of microdroplets at an estimated cooling rate of $10^4$ K $s^{-1}$[153] and cooling at high pressure.[154] As discussed in Sec. IV, PIA does not yield seed-free amorphous ice without annealing procedures. The remnant tiny crystallites are considered to facilitate the crystallization. However, this crystallization pressure is also lower than ~4 GPa of pure ice on similar procedures.[136,143] A kind of impurity ice containing some LiCl is considered to facilitate the crystallization, but the actual contribution is ambiguous. Related to the ion-containing ice, similar procedures starting with ice I can result in the formation of ice VII′ for some ionic species (KCl and RbCl) at quite low pressure ~0.8 GPa.[145,157] These are slightly different stories because ice I directly transformed into ice VII′ during compression at 77 K. Following the arguments for the preference of crystallized ice phase by adding specific organic compounds,[158] ionic species are suspected to facilitate the crystallization of ice VII′, which is somewhat opposite to the studies starting with fully amorphized samples.[151–154] Crystallization consists of processes of nucleation and crystal growth. Ionic species can be considered to affect these processes differently, but the elucidation of the fundamental processes at high pressure is a very hard task, considering the long-standing challenges even at ambient conditions.

## VI. DISCUSSION AND CONCLUSIONS

Nucleation of ice is of importance in many fields, for instance, in biology[159] for the survival of plants and animals at subzero temperatures, in cloud physics,[160] or in industry, e.g., for the prevention of icing on aeroplanes[161,162] or windshields of cars and for the making of technical snow.[163] In all these fields, it is heterogeneous nucleation in supercooled water that is of foremost relevance. For this reason, the field of ice nucleating agents has received much attention.[164,165] Based on most experiments on small droplets of water, the rates for homogeneous nucleation, without any ice nucleating agents,[166] have been measured in experiments, down to temperatures of 225 K (see Fig. 5).

The field of nucleation in amorphous ices is probably equally important, but much less mature. Rates of crystal growth in amorphous ices are of special importance in astrophysical processes, e.g., to understand outgassing of comets or to understand the chemistry behind the evolution of molecules that are buried in amorphous ice and protected from high energy irradiation.[2,167] In addition, in technology, amorphous ices are of importance. Amorphous ices are, for instance, key in the technique of cryo-electron microscopy, where the 2017 Nobel Prize in Chemistry was awarded for "developing cryo-electron microscopy for the high-resolution structure determination of biomolecules in solution."[168] Most notably, the key challenge in cryo-electron microscopy is to avoid ice crystallization at cryo-temperatures far below the ice freezing point.[169] Such low temperatures are beneficial because of lower thermal motion and, hence, higher resolution, but require the aqueous samples to be protected in a matrix of amorphous ice (specifically, hyperquenched glassy water). Crystalline ice, by contrast to amorphous ice, destroys the cells, proteins, etc., to be studied, and so the knowledge of rates of nucleation and growth of ice both upon cooling is central for the success of studying an aqueous sample in the electron beam at cryogenic temperatures.

Nucleation rates in deeply supercooled water at temperatures between 130 and 225 K are notoriously difficult to measure. Only in the last few years, clever and cumbersome experimental approaches involving laser heating were devised by Kimmel *et al.*[62] and Xu *et al.*,[59] who were able to carefully separate nucleation rates from growth rates in thin amorphous films (of 15–240 nm thickness) at 190–225 K. Their nucleation rates connect nicely with the droplet nucleation rates, as shown in Fig. 5, where a maximum near 215 K was observed. Yet, these pioneering results may not be the final answer. It still remains unclear what the effect of preparation conditions and, hence, microporosity or impurities taken up during deposition are on these rates. Such vapor-deposited nm-films (or thicker samples) of ASW not being fully characterized in most experiments are one of the issues in the field. Depending on substrate temperature, background pressure, direction of deposition employed, vapor pressures during deposition, etc., the sample may be very different.

Some samples may feature a huge amount of micropores (of typically 2 nm in diameter), others may contain trapped molecules in such micropores and even others might be much less compact, but contain some fraction of crystalline ice. Methods to probe impurities or to measure porosities exist, but are often not feasible in studies devised to study nucleation and growth rates. This means that it is very hard to compare studies done in different laboratories, even different studies done in a single research group. In such vapor-deposited films, the question whether the nucleation starts at the external surface, the internal surface, or within the bulk is answered differently in different studies. In addition, the thickness of the film has a tremendous impact, where rates of crystallization in films thinner than about 5 nm are limited by ice nucleation, reach a plateau for somewhat thicker films, and finally change again in even thicker films.

In the case of hyperquenched glassy water produced by ultrafast cooling of liquid droplets, the issue of microporosity is absent. Yet, there are similar problems about characterizing the samples, especially the degree of crystallinity or the number of pre-existing nuclei after deposition and vitrification of the droplets. This is easily evident when comparing the crystallization kinetics in three deposits by Maté *et al.*[10] Their deposits at 40 and 90 K crystallize much more rapidly than the deposit at 14 K. The Avrami exponent obtained from isothermal crystallization experiments in their films is about 2.4 for the former, but only 1.4 for the latter. This suggests that the former two deposits suffer from some crystallinity present in the deposits even before doing the isothermal experiment, whereas there is much less or no crystallinity in the 14 K deposit. Even though Maté *et al.* did not apply any technique devised at characterizing the level of crystallinity or the presence of seeds, their results clearly show that their initial deposits differ in this respect. The key issue here is that vitrification needs to be done at rates as high as possible to avoid crystallinity or seeds, at least of $10^7$ K $s^{-1}$.[97] The highest cooling rates in the literature were reached in the studies by Hage *et al.*,[106] who studied the crystallization kinetics based on IR spectroscopy. Even in their study, it was not possible to separate ice nucleation from crystal growth so that the combined process of crystallization was investigated even by them. Yet, these experiments are most closely related to simulations, where the work by Moore and Molinero on mW water follows the experimental procedures.[103] Encouragingly, the Avrami exponents found in experiments and simulations match quite nicely. This at least suggests that the stages of crystallization as observed in simulations (see Fig. 7) are also found in the vitrified droplets. Yet, the role of the interfaces between droplets (see Fig. 9) remains unclear. Such interfaces between $\mu$m-sized droplets have not been considered in simulations, and from the experimental point of view, it is still unclear what their role is. Possibly, the droplets coalesce prior to crystallization, and possibly, ice nucleation even starts at the interfaces. These questions will need to be answered in future work.

Yet, another important aspect of why to study amorphous ices near their crystallization temperatures is "polyamorphism" and the connection of amorphous ices with liquid counterparts at higher temperatures. At such higher temperatures, polyamorphism may develop into a first-order liquid–liquid transition in $H_2O$. That is, it is of fundamental importance to understand whether amorphous ices turn into deeply supercooled liquid prior to crystallization or whether crystallization takes place in the amorphous solid. This question requires the study of crystallization at elevated temperatures, up to about 0.5 GPa for the study of HDA/LDA polyamorphism and the possible HDL/LDL first-order transition, and studies above 0.8 GPa for the study of HDA/VHDA polyamorphism. Investigation of the pre-existence of ice nuclei in the GPa-domain is even more challenging than the studies at ambient pressure or in the vacuum carried out on HGW or ASW. To separate nucleation rates and crystal growth rates is currently out of reach. Only in a handful studies, actually crystallization rates could be reported, most notably in the studies by Handle and Loerting[135] and Stern *et al.*[31] (see Figs. 11 and 12). Both of these studies agree on that there is a dynamic anomaly near 0.8 GPa, which signifies the pressure region where there is a sharp change in the coordination number from 4+1 in HDA to 4+2 in VHDA. However, the absolute values and even the qualitative trends are different, where much higher rates are extracted in the study by Handle and Loerting, which indicates that these results were affected by incomplete amorphization and incomplete annealing out of crystalline nuclei, by contrast to the results by Stern *et al.* Most other studies remain at the more qualitative level of the determination of $T_x$. Quite interestingly, $T_x$ shows a maximum near 1.8 GPa at about 183 K in the domain of VHDA. The question about the highest pressure at which amorphous ice may exist is unclear—according to Fig. 13, this may be as high as 5.5 GPa, but may also be near 4 GPa. The incorporation of salts has a very significant impact on crystallization in the pressure range above 2 GPa, but not so at lower pressures. This is owing to the possibility of incorporating salts into the ice VII′ structure into which amorphous ice crystallizes above 2 GPa. Below 2 GPa, amorphous ice crystallizes into a range of different high-pressure polymorphs, where typically there is a competition between two types of crystallization so that mixtures of high-pressure polymorphs result, e.g., mixtures of ice IV and ice XII when crystallizing at 1 GPa. There is always one type of crystallization that is slow but commences at low temperature and a second type that is much faster but commences at higher temperatures. By changing experimental parameters, especially the heating rate, it is possible to govern the crystallization and suppress the secondary polymorph. To make ice XII and avoid ice IV, rapid heating (e.g., 30 K $min^{-1}$) is necessary, whereas very slow heating (e.g., 0.1 K $min^{-1}$) is necessary to make pure ice IV. Even though it is clear that there are qualitatively two types of crystallization, a quantification of rates and a separation of nucleation and growth have not been possible.

To wrap up, this Review shows that there are still considerable gaps in our knowledge about nucleation of ice in amorphous water. These are owing to the difficulty in making the amorphous ices and to characterizing them thoroughly, especially regarding pre-existing nuclei and crystallinity. In the field of ice nucleation from the liquid, quite a lot of work has been devoted to both homogeneous and heterogeneous nucleation. Even under high-pressure conditions near 1 GPa, nucleating agents have been studied to try to crystallize ice IV selectively from the liquid.[158,170] By contrast, there is basically nothing known about heterogeneous nucleation in amorphous ices/deeply supercooled water. The impact of nucleating agents or agents suppressing nucleation has simply not been studied at all. Even homogeneous nucleation is not understood, where the separation of rates of nucleation from the rates of growth has mostly been impossible, except for the pioneering studies mentioned above. That is, much future work is required, especially what regards preparation

of samples that are free from ice nuclei so that highest temperatures can be reached before crystallization sets in. This was the aim of the study of Stern *et al.*,[31] who deduced from their results that in the pressure range up to 0.3 GPa, crystallization actually takes place from the deeply supercooled liquid, whereas above 0.3 GPa, crystallization takes place from the amorphous solid.

## ACKNOWLEDGMENTS

We are indebted to all the colleagues, whose work on amorphous ices and supercooled water has inspired us over the years, including (in alphabetical order) Katrin Amann-Winkel, C. Austen Angell, Livia Bove, Roland Böhmer, Pablo G. Debenedetti, Erwin Mayer, Osamu Mishima, and H. Eugene Stanley. Continuous support of amorphous ice research by the Austrian Science Fund FWF (START-award, bilateral projects and standalone projects) and the European Research Council ERC (Starting Grant SULIWA) is gratefully acknowledged by T.L. Our current research was supported by the Centre for Molecular Water Science (CMWS, DESY Hamburg) in an Early Science Project. C.M.T. received a DOC fellowship of the Austrian Academy of Sciences ÖAW and was supported by the Early Stage Funding 2021 of the University of Innsbruck. K.Y. is a recipient of an overseas research fellowship by the Japan Society for the Promotion of Science (JSPS).

## AUTHOR DECLARATIONS

### Conflict of Interest

The authors have no conflicts to disclose.

### Author Contributions

All authors contributed equally to this Review. C.M.T. identified and reviewed ASW literature, wrote the section on ASW, designed Figs. 1–5, took the lead in putting together all parts of the review and made corrections in all sections. L.R.F. identified and reviewed literature on LDA/HDA/VHDA below 2 GPa, wrote the section about amorphous ices up to 2 GPa and designed Figs. 11 and 12. J.G. identified and reviewed HGW literature, wrote the chapter on HGW and designed Figs. 6–8. K.Y. identified and reviewed literature on HDA/VHDA above 2 GPa, wrote the section about amorphous ices above 2 GPa and designed Figs. 10 and 13. T.L. provided the concept for this review article, wrote the Introduction and Conclusions sections and contributed to all other sections.

**Christina M. Tonauer**: Visualization (equal); Writing – original draft (equal); Writing – review & editing (equal). **Lilli-Ruth Fidler**: Visualization (equal); Writing – original draft (equal); Writing – review & editing (equal). **Johannes Giebelmann**: Visualization (equal); Writing – original draft (equal); Writing – review & editing (equal). **Keishiro Yamashita**: Visualization (equal); Writing – original draft (equal); Writing – review & editing (equal). **Thomas Loerting**: Conceptualization (lead); Funding acquisition (lead); Visualization (equal); Writing – original draft (lead); Writing – review & editing (lead).

## DATA AVAILABILITY

The data that support the findings of this study are available from the corresponding author upon reasonable request.

## REFERENCES

[1]E. Mayer and R. Pletzer, "Astrophysical implications of amorphous ice—A microporous solid," Nature **319**, 298–301 (1986).
[2]D. J. Burke and W. A. Brown, "Ice in space: Surface science investigations of the thermal desorption of model interstellar ices on dust grain analogue surfaces," Phys. Chem. Chem. Phys. **12**, 5947 (2010).
[3]T. Loerting, K. Winkel, M. Seidl *et al.*, "How many amorphous ices are there?," Phys. Chem. Chem. Phys. **13**, 8783 (2011).
[4]A. Potapov, C. Jäger, and T. Henning, "Ice coverage of dust grains in cold astrophysical environments," Phys. Rev. Lett. **124**, 221103 (2020).
[5]J. K. Davies, T. L. Roush, D. P. Cruikshank *et al.*, "The detection of water ice in comet Hale-Bopp," Icarus **127**, 238–245 (1997).
[6]F. Poulet, D. P. Cruikshank, J. N. Cuzzi *et al.*, "Compositions of Saturn's rings A, B, and C from high resolution near-infrared spectroscopic observations," Astron. Astrophys. **412**, 305–316 (2003).
[7]A. Bar-Nun, J. Dror, E. Kochavi, and D. Laufer, "Amorphous water ice and its ability to trap gases," Phys. Rev. B **35**, 2427–2435 (1987).
[8]M. P. Bernstein, J. P. Dworkin, S. A. Sandford *et al.*, "Racemic amino acids from the ultraviolet photolysis of interstellar ice analogues," Nature **416**, 401–403 (2002).
[9]P. de Marcellus, C. Meinert, M. Nuevo *et al.*, "Non-racemic amino acid production by ultraviolet irradiation of achiral interstellar ice analogs with circularly polarized light," Astrophys. J. **727**, L27 (2011).
[10]B. Maté, Y. Rodríguez-Lazcano, and V. J. Herrero, "Morphology and crystallization kinetics of compact (HGW) and porous (ASW) amorphous water ice," Phys. Chem. Chem. Phys. **14**, 10595 (2012).
[11]J. A. Ghormley, "Adsorption and occlusion of gases by the low-temperature forms of ice," J. Chem. Phys. **46**, 1321–1325 (1967).
[12]E. F. Burton and W. F. Oliver, "X-ray diffraction patterns of ice," Nature **135**, 505–506 (1935).
[13]P. Brüggeller and E. Mayer, "Complete vitrification in pure liquid water and dilute aqueous solutions," Nature **288**, 569–571 (1980).
[14]O. Mishima, L. D. Calvert, and E. Whalley, "'Melting ice' I at 77 K and 10 kbar: A new method of making amorphous solids," Nature **310**, 393–395 (1984).
[15]T. Loerting, C. Salzmann, I. Kohl *et al.*, "A second distinct structural 'state' of high-density amorphous ice at 77 K and 1 bar," Phys. Chem. Chem. Phys. **3**, 5355–5357 (2001).
[16]T. Loerting, M. Bauer, I. Kohl *et al.*, "Cryoflotation: Densities of amorphous and crystalline ices," J. Phys. Chem. B **115**, 14167–14175 (2011).
[17]C. A. Tulk, C. J. Benmore, J. Urquidi *et al.*, "Structural studies of several distinct metastable forms of amorphous ice," Science **297**, 1320–1323 (2002).
[18]J. Urquidi, C. J. Benmore, P. A. Egelstaff *et al.*, "A structural comparison of supercooled water and intermediate density amorphous ices," Mol. Phys. **102**, 2007–2014 (2004).
[19]J. S. Tse, D. D. Klug, M. Guthrie *et al.*, "Investigation of the intermediate- and high-density forms of amorphous ice by molecular dynamics calculations and diffraction experiments," Phys. Rev. B **71**, 214107 (2005).
[20]A. Rosu-Finsen, M. B. Davies, A. Amon *et al.*, "Medium-density amorphous ice," Science **379**, 474–478 (2023).
[21]D. T. Bowron, J. L. Finney, A. Hallbrucker *et al.*, "The local and intermediate range structures of the five amorphous ices at 80 K and ambient pressure: A Faber-Ziman and Bhatia-Thornton analysis," J. Chem. Phys. **125**, 194502 (2006).
[22]O. Mishima, L. D. Calvert, and E. Whalley, "An apparently first-order transition between two amorphous phases of ice induced by pressure," Nature **314**, 76–78 (1985).
[23]S. Lemke, P. H. Handle, L. J. Plaga *et al.*, "Relaxation dynamics and transformation kinetics of deeply supercooled water: Temperature, pressure, doping, and proton/deuteron isotope effects," J. Chem. Phys. **147**, 034506 (2017).
[24]M. S. Elsaesser, K. Winkel, E. Mayer, and T. Loerting, "Reversibility and isotope effect of the calorimetric glass → liquid transition of low-density amorphous ice," Phys. Chem. Chem. Phys. **12**, 708–712 (2010).
[25]M. Seidl, M. S. Elsaesser, K. Winkel *et al.*, "Volumetric study consistent with a glass-to-liquid transition in amorphous ices under pressure," Phys. Rev. B **83**, 100201 (2011).

[26]V. Fuentes-Landete, L. J. Plaga, M. Keppler *et al.*, "Nature of water's second glass transition elucidated by doping and isotope substitution experiments," Phys. Rev. X **9**, 011015 (2019).
[27]K. Amann-Winkel, R. Böhmer, F. Fujara *et al.*, "*Colloquium*: Water's controversial glass transitions," Rev. Mod. Phys. **88**, 011002 (2016).
[28]P. H. Poole, F. Sciortino, U. Essmann, and H. E. Stanley, "Phase behaviour of metastable water," Nature **360**, 324–328 (1992).
[29]C. A. Angell, "Insights into phases of liquid water from study of its unusual glass-forming properties," Science **319**, 582–587 (2008).
[30]P. Gallo, K. Amann-Winkel, C. A. Angell *et al.*, "Water: A tale of two liquids," Chem. Rev. **116**, 7463–7500 (2016).
[31]J. N. Stern, M. Seidl-Nigsch, and T. Loerting, "Evidence for high-density liquid water between 0.1 and 0.3 GPa near 150 K," Proc. Natl. Acad. Sci. U. S. A. **116**, 9191–9196 (2019).
[32]C. R. Hill, C. Mitterdorfer, T. G. A. Youngs *et al.*, "Neutron scattering analysis of water's glass transition and micropore collapse in amorphous solid water," Phys. Rev. Lett. **116**, 215501 (2016).
[33]M. Avrami, "Kinetics of phase change. I. General theory," J. Chem. Phys. **7**, 1103–1112 (1939).
[34]M. Avrami, "Kinetics of phase change. II. Transformation-time relations for random distribution of nuclei," J. Chem. Phys. **8**, 212–224 (1940).
[35]M. Avrami, "Granulation, phase change, and microstructure kinetics of phase change. III," J. Chem. Phys. **9**, 177–184 (1941).
[36]A. N. Kolmogorov, "On the statistical theory of crystallization of metals," Bull Acad. Sci. USSR **1**, 355–359 (1937) (in Russian).
[37]A. A. Burbelko, E. Fraś, and W. Kapturkiewicz, "About Kolmogorov's statistical theory of phase transformation," Mater. Sci. Eng.: A **413-414**, 429–434 (2005).
[38]W. A. Johnson and R. Mehl, "Reaction kinetics in processes of nucleation and growth," Am. Inst. Min. Metall. Eng. **135**, 416–458 (1939).
[39]H. R. Pruppacher and J. D. Klett, *Microphysics of Clouds and Precipitation* (Reidel, Dordrecht, 1980).
[40]H. Laksmono, T. A. McQueen, J. A. Sellberg *et al.*, "Anomalous behavior of the homogeneous ice nucleation rate in 'no-man's land,'" J. Phys. Chem. Lett. **6**, 2826–2832 (2015).
[41]J. D. Atkinson, B. J. Murray, and D. O'Sullivan, "Rate of homogenous nucleation of ice in supercooled water," J. Phys. Chem. A **120**, 6513–6520 (2016).
[42]T. Koop and B. J. Murray, "A physically constrained classical description of the homogeneous nucleation of ice in water," J. Chem. Phys. **145**, 211915 (2016).
[43]P. Jenniskens and D. F. Blake, "Crystallization of amorphous water ice in the solar system," Astrophys. J. **473**, 1104–1113 (1996).
[44]R. S. Smith, C. Huang, E. K. L. Wong, and B. D. Kay, "Desorption and crystallization kinetics in nanoscale thin films of amorphous water ice," Surf. Sci. **367**, L13–L18 (1996).
[45]V. Buch, L. Delzeit, C. Blackledge, and J. P. Devlin, "Structure of the ice nanocrystal surface from simulated versus experimental spectra of adsorbed $CF_4$," J. Phys. Chem. **100**, 3732–3744 (1996).
[46]R. S. Smith and B. D. Kay, "Molecular beam studies of kinetic processes in nanoscale water films," Surf. Rev. Lett. **04**, 781–797 (1997).
[47]Z. Dohnálek, R. L. Ciolli, G. A. Kimmel *et al.*, "Substrate induced crystallization of amorphous solid water at low temperatures," J. Chem. Phys. **110**, 5489–5492 (1999).
[48]Z. Dohnálek, G. A. Kimmel, R. L. Ciolli *et al.*, "The effect of the underlying substrate on the crystallization kinetics of dense amorphous solid water films," J. Chem. Phys. **112**, 5932–5941 (2000).
[49]P. Löfgren, P. Ahlström, D. V. Chakarov *et al.*, "Substrate dependent sublimation kinetics of mesoscopic ice films," Surf. Sci. **367**, L19–L25 (1996).
[50]D. J. Safarik, R. J. Meyer, and C. B. Mullins, "Thickness dependent crystallization kinetics of sub-micron amorphous solid water films," J. Chem. Phys. **118**, 4660–4671 (2003).
[51]D. J. Safarik and C. B. Mullins, "The nucleation rate of crystalline ice in amorphous solid water," J. Chem. Phys. **121**, 6003–6010 (2004).
[52]E. H. G. Backus, M. L. Grecea, A. W. Kleyn, and M. Bonn, "Surface crystallization of amorphous solid water," Phys. Rev. Lett. **92**, 236101 (2004).
[53]T. Kondo, H. S. Kato, M. Bonn, and M. Kawai, "Deposition and crystallization studies of thin amorphous solid water films on Ru(0001) and on CO-precovered Ru(0001)," J. Chem. Phys. **127**, 094703 (2007).
[54]T. Yamauchi, K. Mine, Y. Nakashima *et al.*, "Crystallization of $D_2O$ thin films on Ru(001) surfaces," Appl. Surf. Sci. **256**, 1124–1127 (2009).
[55]R. S. Smith, J. Matthiesen, J. Knox, and B. D. Kay, "Crystallization kinetics and excess free energy of $H_2O$ and $D_2O$ nanoscale films of amorphous solid water," J. Phys. Chem. A **115**, 5908–5917 (2011).
[56]S. Townrow and P. G. Coleman, "Structural changes in amorphous solid water films on heating to 120–140 K and 150–160 K seen by positronium annihilation spectroscopy," J. Phys.: Condens. Matter **27**, 225401 (2015).
[57]Y. Xu, N. G. Petrik, R. S. Smith *et al.*, "Growth rate of crystalline ice and the diffusivity of supercooled water from 126 to 262 K," Proc. Natl. Acad. Sci. U. S. A. **113**, 14921–14925 (2016).
[58]C. Yuan, R. S. Smith, and B. D. Kay, "Surface and bulk crystallization of amorphous solid water films: Confirmation of 'top-down' crystallization," Surf. Sci. **652**, 350–354 (2016).
[59]Y. Xu, N. G. Petrik, R. S. Smith *et al.*, "Homogeneous nucleation of ice in transiently-heated, supercooled liquid water films," J. Phys. Chem. Lett. **8**, 5736–5743 (2017).
[60]E. H. Mitchell, U. Raut, B. D. Teolis, and R. A. Baragiola, "Porosity effects on crystallization kinetics of amorphous solid water: Implications for cold icy objects in the outer solar system," Icarus **285**, 291–299 (2017).
[61]R. S. Smith, C. Yuan, N. G. Petrik *et al.*, "Crystallization growth rates and front propagation in amorphous solid water films," J. Chem. Phys. **150**, 214703 (2019).
[62]G. A. Kimmel, Y. Xu, A. Brumberg *et al.*, "Homogeneous ice nucleation rates and crystallization kinetics in transiently-heated, supercooled water films from 188 K to 230 K," J. Chem. Phys. **150**, 204509 (2019).
[63]K. Harada, T. Sugimoto, F. Kato *et al.*, "Thickness dependent homogeneous crystallization of ultrathin amorphous solid water films," Phys. Chem. Chem. Phys. **22**, 1963–1973 (2020).
[64]P. Löfgren, P. Ahlström, J. Lausma *et al.*, "Crystallization kinetics of thin amorphous water films on surfaces," Langmuir **19**, 265–274 (2003).
[65]E. Mayer and R. Pletzer, "Amorphous ice. A microporous solid: Astrophysical implications," J. Phys., Colloq. **48**, C1-581–C1-586 (1987).
[66]K. P. Stevenson, G. A. Kimmel, Z. Dohnálek *et al.*, "Controlling the morphology of amorphous solid water," Science **283**, 1505–1507 (1999).
[67]G. A. Kimmel, K. P. Stevenson, Z. Dohnálek *et al.*, "Control of amorphous solid water morphology using molecular beams. I. Experimental results," J. Chem. Phys. **114**, 5284–5294 (2001).
[68]G. A. Kimmel, Z. Dohnálek, K. P. Stevenson *et al.*, "Control of amorphous solid water morphology using molecular beams. II. Ballistic deposition simulations," J. Chem. Phys. **114**, 5295–5303 (2001).
[69]Z. Dohnálek, G. A. Kimmel, P. Ayotte *et al.*, "The deposition angle-dependent density of amorphous solid water films," J. Chem. Phys. **118**, 364–372 (2003).
[70]C. Mitterdorfer, M. Bauer, T. G. A. Youngs *et al.*, "Small-angle neutron scattering study of micropore collapse in amorphous solid water," Phys. Chem. Chem. Phys. **16**, 16013–16020 (2014).
[71]R. A. Baragiola, "Microporous amorphous water ice thin films: Properties and their astronomical implications," in *Water in Confining Geometries*, edited by V. Buch and J. P. Devlin (Springer, Berlin, Heidelberg, 2003), pp. 359–395.
[72]C. Yuan, R. S. Smith, and B. D. Kay, "Communication: Distinguishing between bulk and interface-enhanced crystallization in nanoscale films of amorphous solid water," J. Chem. Phys. **146**, 031102 (2017).
[73]D. J. Safarik and C. B. Mullins, "Surface phase transformation kinetics: A geometrical model for thin films of nonvolatile and volatile solids," J. Chem. Phys. **117**, 8110–8123 (2002).
[74]L. Lupi, A. Hudait, B. Peters *et al.*, "Role of stacking disorder in ice nucleation," Nature **551**, 218–222 (2017).
[75]B. Rowland, N. S. Kadagathur, J. P. Devlin *et al.*, "Infrared spectra of ice surfaces and assignment of surface-localized modes from simulated spectra of cubic ice," J. Chem. Phys. **102**, 8328–8341 (1995).
[76]G. Zimbitas and A. Hodgson, "The morphology of thin water films on Pt(111) probed by chloroform adsorption," Chem. Phys. Lett. **417**, 1–5 (2006).

[77]D. H. Lee and H. Kang, "Acid-promoted crystallization of amorphous solid water," J. Phys. Chem. C **122**, 24164–24170 (2018).
[78]S. Gärtner, T. F. Headen, T. G. A. Youngs *et al.*, "Nanoscale structure of amorphous solid water: What determines the porosity in ASW?," Proc. Int. Astron. Union **15**, 368–369 (2019).
[79]R. S. Smith, T. Zubkov, and B. D. Kay, "The effect of the incident collision energy on the phase and crystallization kinetics of vapor deposited water films," J. Chem. Phys. **124**, 114710 (2006).
[80]I. de Almeida Ribeiro, M. de Koning, and V. Molinero, "Is it possible to follow the structural evolution of water in 'no-man's land' using a pulsed-heating procedure?," J. Phys. Chem. Lett. **13**, 1085–1089 (2022).
[81]W. Hagen, A. G. G. M. Tielens, and J. M. Greenberg, "The infrared spectra of amorphous solid water and ice $I_c$ between 10 and 140 K," Chem. Phys. **56**, 367–379 (1981).
[82]S. E. Wood, M. B. Baker, and B. D. Swanson, "Instrument for studies of homogeneous and heterogeneous ice nucleation in free-falling supercooled water droplets," Rev. Sci. Instrum. **73**, 3988–3996 (2002).
[83]M. E. Earle, T. Kuhn, A. F. Khalizov, and J. J. Sloan, "Volume nucleation rates for homogeneous freezing in supercooled water microdroplets: Results from a combined experimental and modelling approach," Atmos. Chem. Phys. **10**, 7945–7961 (2010).
[84]B. Riechers, F. Wittbracht, A. Hütten, and T. Koop, "The homogeneous ice nucleation rate of water droplets produced in a microfluidic device and the role of temperature uncertainty," Phys. Chem. Chem. Phys. **15**, 5873 (2013).
[85]P. Kabath, P. Stöckel, A. Lindinger, and H. Baumgärtel, "The nucleation of ice in supercooled $D_2O$ and $H_2O$," J. Mol. Liq. **125**, 204–211 (2006).
[86]S. M. A. Malek, F. Sciortino, P. H. Poole, and I. Saika-Voivod, "Evaluating the Laplace pressure of water nanodroplets from simulations," J. Phys.: Condens. Matter **30**, 144005 (2018).
[87]T. Li, D. Donadio, and G. Galli, "Ice nucleation at the nanoscale probes no man's land of water," Nat. Commun. **4**, 1887 (2013).
[88]V. Molinero and E. B. Moore, "Water modeled as an intermediate element between carbon and silicon," J. Phys. Chem. B **113**, 4008–4016 (2009).
[89]E. B. Moore and V. Molinero, "Structural transformation in supercooled water controls the crystallization rate of ice," Nature **479**, 506–508 (2011).
[90]A. Haji-Akbari and P. G. Debenedetti, "Perspective: Surface freezing in water: A nexus of experiments and simulations," J. Chem. Phys. **147**, 060901 (2017).
[91]C. A. Angell, "Liquid fragility and the glass transition in water and aqueous solutions," Chem. Rev. **102**, 2627–2650 (2002).
[92]J. Bachler, P. H. Handle, N. Giovambattista, and T. Loerting, "Glass polymorphism and liquid–liquid phase transition in aqueous solutions: Experiments and computer simulations," Phys. Chem. Chem. Phys. **21**, 23238–23268 (2019).
[93]N. H. Fletcher, "Structural aspects of the ice-water system," Rep. Prog. Phys. **34**, 913–994 (1971).
[94]C. A. Angell and E. J. Sare, "Glass-forming composition regions and glass transition temperatures for aqueous electrolyte solutions," J. Chem. Phys. **52**, 1058–1068 (1970).
[95]E. Mayer, "New method for vitrifying water and other liquids by rapid cooling of their aerosols," J. Appl. Phys. **58**, 663–667 (1985).
[96]J. Bachler, J. Giebelmann, and T. Loerting, "Experimental evidence for glass polymorphism in vitrified water droplets," Proc. Natl. Acad. Sci. U. S. A. **118**, e2108194118 (2021).
[97]I. Kohl, L. Bachmann, A. Hallbrucker *et al.*, "Liquid-like relaxation in hyperquenched water at ≤140 K," Phys. Chem. Chem. Phys. **7**, 3210 (2005).
[98]L. Xu, P. Kumar, S. V. Buldyrev *et al.*, "Relation between the Widom line and the dynamic crossover in systems with a liquid–liquid phase transition," Proc. Natl. Acad. Sci. U. S. A. **102**, 16558–16562 (2005).
[99]A. Hallbrucker and E. Mayer, "Calorimetric study of the vitrified liquid water to cubic ice phase transition," J. Phys. Chem. **91**, 503–505 (1987).
[100]A. Hallbrucker, E. Mayer, and G. P. Johari, "The heat capacity and glass transition of hyperquenched glassy water," Philos. Mag. B **60**, 179–187 (1989).
[101]G. P. Johari, A. Hallbrucker, and E. Mayer, "The glass–liquid transition of hyperquenched water," Nature **330**, 552–553 (1987).
[102]G. P. Johari, A. Hallbrucker, and E. Mayer, "Isotope effect on the glass transition and crystallization of hyperquenched glassy water," J. Chem. Phys. **92**, 6742–6746 (1990).
[103]E. B. Moore and V. Molinero, "Ice crystallization in water's 'no-man's land,'" J. Chem. Phys. **132**, 244504 (2010).
[104]E. B. Moore and V. Molinero, "Is it cubic? Ice crystallization from deeply supercooled water," Phys. Chem. Chem. Phys. **13**, 20008 (2011).
[105]W. Hage, A. Hallbrucker, E. Mayer, and G. P. Johari, "Crystallization kinetics of water below 150 K," J. Chem. Phys. **100**, 2743–2747 (1994).
[106]W. Hage, A. Hallbrucker, E. Mayer, and G. P. Johari, "Kinetics of crystallizing $D_2O$ water near 150 K by Fourier transform infrared spectroscopy and a comparison with the corresponding calorimetric studies on $H_2O$ water," J. Chem. Phys. **103**, 545–550 (1995).
[107]J. S. Blázquez, F. J. Romero, C. F. Conde *et al.*, "A review of different models derived from classical Kolmogorov, Johnson and Mehl, and Avrami (KJMA) theory to recover physical meaning in solid-state transformations," Phys. Status Solidi B **259**, 2100524 (2022).
[108]C. Lin, J. S. Smith, S. V. Sinogeikin, and G. Shen, "Experimental evidence of low-density liquid water upon rapid decompression," Proc. Natl. Acad. Sci. U. S. A. **115**, 2010–2015 (2018).
[109]R. J. Nelmes, J. S. Loveday, T. Strässle *et al.*, "Annealed high-density amorphous ice under pressure," Nat. Phys. **2**, 414–418 (2006).
[110]K. Winkel, E. Mayer, and T. Loerting, "Equilibrated high-density amorphous ice and its first-order transition to the low-density form," J. Phys. Chem. B **115**, 14141–14148 (2011).
[111]M. Seidl, K. Amann-Winkel, P. H. Handle *et al.*, "From parallel to single crystallization kinetics in high-density amorphous ice," Phys. Rev. B **88**, 174105 (2013).
[112]M. Seidl, A. Fayter, J. N. Stern *et al.*, "Shrinking water's no man's land by lifting its low-temperature boundary," Phys. Rev. B **91**, 144201 (2015).
[113]C. M. Tonauer, M. Seidl-Nigsch, and T. Loerting, "High-density amorphous ice: Nucleation of nanosized low-density amorphous ice," J. Phys.: Condens. Matter **30**, 034002 (2018).
[114]C. M. Tonauer, *Glassy Nuclei in Amorphous Ice: Novel Evidence for the Two-Liquids Nature of Water* (Springer Fachmedien Wiesbaden, 2019).
[115]P. H. Handle, T. Loerting, and F. Sciortino, "Supercooled and glassy water: Metastable liquid(s), amorphous solid(s), and a no-man's land," Proc. Natl. Acad. Sci. U. S. A. **114**, 13336–13344 (2017).
[116]K. Winkel, D. T. Bowron, T. Loerting *et al.*, "Relaxation effects in low density amorphous ice: Two distinct structural states observed by neutron diffraction," J. Chem. Phys. **130**, 204502 (2009).
[117]P. H. Handle and T. Loerting, "Temperature-induced amorphisation of hexagonal ice," Phys. Chem. Chem. Phys. **17**, 5403–5412 (2015).
[118]Y. Wang, H. Zhang, X. Yang *et al.*, "Kinetic boundaries and phase transformations of ice i at high pressure," J. Chem. Phys. **148**, 044508 (2018).
[119]S. Klotz, J. M. Besson, G. Hamel *et al.*, "Metastable ice VII at low temperature and ambient pressure," Nature **398**, 681–684 (1999).
[120]D. D. Klug, Y. P. Handa, J. S. Tse, and E. Whalley, "Transformation of ice VIII to amorphous ice by 'melting' at low temperature," J. Chem. Phys. **90**, 2390–2392 (1989).
[121]J. J. Shephard, S. Klotz, M. Vickers, and C. G. Salzmann, "A new structural relaxation pathway of low-density amorphous ice," J. Chem. Phys. **144**, 204502 (2016).
[122]Y. Yoshimura, S. T. Stewart, M. Somayazulu *et al.*, "High-pressure x-ray diffraction and Raman spectroscopy of ice VIII," J. Chem. Phys. **124**, 024502 (2006).
[123]C. Lin, X. Liu, X. Yong *et al.*, "Temperature-dependent kinetic pathways featuring distinctive thermal-activation mechanisms in structural evolution of ice VII," Proc. Natl. Acad. Sci. U. S. A. **117**, 15437–15442 (2020).
[124]C. Lin, X. Yong, J. S. Tse *et al.*, "Kinetically controlled two-step amorphization and amorphous-amorphous transition in ice," Phys. Rev. Lett. **119**, 135701 (2017).
[125]P. H. Handle and T. Loerting, "Experimental study of the polyamorphism of water. II. The isobaric transitions between HDA and VHDA at intermediate and high pressures," J. Chem. Phys. **148**, 124509 (2018).

[126]M. Ladd-Parada, K. Amann-Winkel, K. H. Kim *et al.*, "Following the crystallization of amorphous ice after ultrafast laser heating," J. Phys. Chem. B **126**, 2299–2307 (2022).
[127]O. Mishima, K. Takemura, and K. Aoki, "Visual observations of the amorphous-amorphous transition in $H_2O$ under pressure," Science **254**, 406–408 (1991).
[128]D. Mariedahl, F. Perakis, A. Späh *et al.*, "X-ray studies of the transformation from high- to low-density amorphous water," Philos. Trans. R. Soc., A **377**, 20180164 (2019).
[129]M. M. Koza, H. Schober, T. Hansen *et al.*, "Ice XII in its second regime of metastability," Phys. Rev. Lett. **84**, 4112–4115 (2000).
[130]S. Klotz, G. Hamel, J. S. Loveday *et al.*, "Recrystallisation of HDA ice under pressure by in-situ neutron diffraction to 3.9 GPa," Z. Kristallogr. - Cryst. Mater. **218**, 117–122 (2003).
[131]C. G. Salzmann, T. Loerting, I. Kohl *et al.*, "Pure ice IV from high-density amorphous ice," J. Phys. Chem. B **106**, 5587–5590 (2002).
[132]I. Kohl, E. Mayer, and A. Hallbrucker, "Ice XII forms on compression of hexagonal ice at 77 K via high-density amorphous water," Phys. Chem. Chem. Phys. **3**, 602–605 (2001).
[133]T. Loerting, I. Kohl, C. Salzmann *et al.*, "Metastability domain of ice XII revealed between 158–212 K and 0.7–1.5 GPa on isobaric heating of high-density amorphous ice," J. Chem. Phys. **116**, 3171–3174 (2002).
[134]C. G. Salzmann, E. Mayer, and A. Hallbrucker, "Effect of heating rate and pressure on the crystallization kinetics of high-density amorphous ice on isobaric heating between 0.2 and 1.9 GPa," Phys. Chem. Chem. Phys. **6**, 5156 (2004).
[135]P. H. Handle and T. Loerting, "Dynamics anomaly in high-density amorphous ice between 0.7 and 1.1 GPa," Phys. Rev. B **93**, 064204 (2016).
[136]R. J. Hemley, L. C. Chen, and H. K. Mao, "New transformations between crystalline and amorphous ice," Nature **338**, 638–640 (1989).
[137]H. S. Cao, "Formation and crystallization of low-density amorphous ice," J. Phys. D: Appl. Phys. **54**, 203002 (2021).
[138]K. H. Kim, K. Amann-Winkel, N. Giovambattista *et al.*, "Experimental observation of the liquid-liquid transition in bulk supercooled water under pressure," Science **370**, 978–982 (2020).
[139]J. A. Sellberg, C. Huang, T. A. McQueen *et al.*, "Ultrafast X-ray probing of water structure below the homogeneous ice nucleation temperature," Nature **510**, 381–384 (2014).
[140]L. B. Skinner, C. J. Benmore, J. C. Neuefeind, and J. B. Parise, "The structure of water around the compressibility minimum," J. Chem. Phys. **141**, 214507 (2014).
[141]S. Klotz, G. Hamel, J. S. Loveday *et al.*, "Structure of high-density amorphous ice under pressure," Phys. Rev. Lett. **89**, 285502 (2002).
[142]Y. Yoshimura, H.-k. Mao, and R. J. Hemley, "Direct transformation of ice VII′ to low-density amorphous ice," Chem. Phys. Lett. **420**, 503–506 (2006).
[143]Y. Yoshimura, S. T. Stewart, M. Somayazulu *et al.*, "Convergent Raman features in high density amorphous ice, ice VII, and ice VIII under pressure," J. Phys. Chem. B **115**, 3756–3760 (2011).
[144]Y. Yoshimura and H. Kanno, "Pressure-induced amorphization of ice in aqueous LiCl solution," J. Phys.: Condens. Matter **14**, 10671–10674 (2002).
[145]Y. Yoshimura, "Overview of the recent studies on high-pressure impurity ices," J. Raman Spectrosc. **53**, 1739–1747 (2022).
[146]J.-A. Queyroux, J.-A. Hernandez, G. Weck *et al.*, "Melting curve and isostructural solid transition in superionic ice," Phys. Rev. Lett. **125**, 195501 (2020).
[147]Y. Peng, F. Wang, Z. Wang *et al.*, "Two-step nucleation mechanism in solid–solid phase transitions," Nat. Mater. **14**, 101–108 (2015).
[148]O. Mishima and H. E. Stanley, "The relationship between liquid, supercooled and glassy water," Nature **396**, 329–335 (1998).
[149]G. W. Lee, W. J. Evans, and C.-S. Yoo, "Crystallization of water in a dynamic diamond-anvil cell: Evidence for ice VII-like local order in supercompressed water," Phys. Rev. B **74**, 134112 (2006).
[150]J.-Y. Chen and C.-S. Yoo, "High density amorphous ice at room temperature," Proc. Natl. Acad. Sci. U. S. A. **108**, 7685–7688 (2011).
[151]S. Klotz, L. E. Bove, T. Strässle *et al.*, "The preparation and structure of salty ice VII under pressure," Nat. Mater. **8**, 405–409 (2009).
[152]S. Klotz, K. Komatsu, F. Pietrucci *et al.*, "Ice VII from aqueous salt solutions: From a glass to a crystal with broken H-bonds," Sci. Rep. **6**, 32040 (2016).
[153]A.-A. Ludl, L. E. Bove, D. Corradini *et al.*, "Probing ice VII crystallization from amorphous NaCl–$D_2O$ solutions at gigapascal pressures," Phys. Chem. Chem. Phys. **19**, 1875–1883 (2017).
[154]K. Komatsu, A. Shinozaki, S. Machida *et al.*, "Crystal structure of magnesium dichloride decahydrate determined by X-ray and neutron diffraction under high pressure," Acta Crystallogr., Sect. B: Struct. Sci., Cryst. Eng. Mater. **71**, 74–80 (2015).
[155]C. G. Salzmann, Z. Sharif, C. L. Bull *et al.*, "Ammonium fluoride as a hydrogen-disordering agent for ice," J. Phys. Chem. C **123**, 16486–16492 (2019).
[156]M. Watanabe, K. Komatsu, F. Noritake, and H. Kagi, "Structural incorporation of $MgCl_2$ into ice VII at room temperature," Jpn. J. Appl. Phys. **56**, 05FB03 (2017).
[157]Y. Yoshimura, H.-k. Mao, and R. J. Hemley, "Transformation of ice in aqueous KCl solution to a high-pressure, low-temperature phase," Chem. Phys. Lett. **400**, 511–514 (2004).
[158]L. F. Evans, "Selective nucleation of the high-pressure ices," J. Appl. Phys. **38**, 4930–4932 (1967).
[159]F. Franks, *Water: A Matrix of Life*, 2nd ed. (Royal Society of Chemistry, Cambridge, UK, 2000).
[160]C. Hoose and O. Möhler, "Heterogeneous ice nucleation on atmospheric aerosols: A review of results from laboratory experiments," Atmos. Chem. Phys. **12**, 9817–9854 (2012).
[161]Y. Cao, W. Tan, and Z. Wu, "Aircraft icing: An ongoing threat to aviation safety," Aerosp. Sci. Technol. **75**, 353–385 (2018).
[162]Y. Shen, X. Wu, J. Tao *et al.*, "Icephobic materials: Fundamentals, performance evaluation, and applications," Prog. Mater. Sci. **103**, 509–557 (2019).
[163]N. Cochet and P. Widehem, "Ice crystallization by *Pseudomonas syringae*," Appl. Microbiol. Biotechnol. **54**, 153–161 (2000).
[164]B. G. Pummer, C. Budke, S. Augustin-Bauditz *et al.*, "Ice nucleation by water-soluble macromolecules," Atmos. Chem. Phys. **15**, 4077–4091 (2015).
[165]N. Maeda, "Brief overview of ice nucleation," Molecules **26**, 392 (2021).
[166]P. G. Debenedetti, "Supercooled and glassy water," J. Phys.: Condens. Matter **15**, R1669 (2003).
[167]K. I. Öberg, "Photochemistry and astrochemistry: Photochemical pathways to interstellar complex organic molecules," Chem. Rev. **116**, 9631–9663 (2016).
[168]The Nobel Prize in Chemistry 2017, NobelPrize.org, Nobel Prize Outreach AB 2023, Saturday, 21 January 2023, https://www.nobelprize.org/prizes/chemistry/2017/summary/.
[169]R. A. Steinbrecht and K. Zierold, *Cryotechniques in Biological Electron Microscopy* (Springer, Berlin, Heidelberg, 1987).
[170]H. Engelhardt and E. Whalley, "Ice IV," J. Chem. Phys. **56**, 2678–2684 (1972).